



Chem Soc Rev

**Rational strategies for proton conductive metal-organic frameworks**

Journal:	<i>Chemical Society Reviews</i>
Manuscript ID	CS-REV-01-2021-000004.R1
Article Type:	Review Article
Date Submitted by the Author:	15-Mar-2021
Complete List of Authors:	Lim, Dae-Woon; Yonsei University - Wonju Campus, Department of Chemistry and Medical Chemistry Kitagawa, Hiroshi; Kyoto University, Department of Chemistry

SCHOLARONE™  
Manuscripts

## ARTICLE

# Rational strategies for proton conductive metal-organic frameworks

Dae-Woon Lim<sup>\*,a</sup> and Hiroshi Kitagawa<sup>\*,b</sup>

Received 00th January 20xx,  
Accepted 00th January 20xx

DOI: 10.1039/x0xx00000x

Since the transition of an energy platform, proton-conducting materials have played a significant role in broad applications for electrochemical devices. In particular, solid-state proton conductors (SSPCs) are emerging as the electrolyte in fuel cells (FC), a promising power generation technology, because of their high performance and safety for operating in a wide range of temperatures. In recent years, proton-conductive porous metal-organic frameworks (MOFs) exhibiting high proton-conducting properties ( $> 10^{-2} \text{ S cm}^{-1}$ ) have been extensively investigated due to their potential application in solid-state electrolyte. Their structural designability, crystallinity, and porosity are beneficial to fabricate a new type of proton conductor, providing a comprehensive conduction mechanism. For the proton-conductive MOFs, each component, such as the metal centres, organic linkers, and pore space, is manipulated by a judicious pre-design strategy or post-synthetic modification to improve the mobile proton concentration with an efficient conducting pathway. In this review, we highlight rational design strategies for highly proton-conductive MOFs in terms of MOF components, with representative examples from recent years. Subsequently, we discuss the challenges and future directions for the design of proton-conductive MOFs.

<sup>a</sup> Department of Chemistry and Medical Chemistry, College of Science and Technology, Yonsei University, 1 Yonseidae-gil, Wonju, Gangwon-do 26493, Republic of Korea

<sup>b</sup> Division of Chemistry, Graduate School of Science, Kyoto University, Kitashirakawa-Oiwakecho, Sakyou-ku, Kyoto 606-8502, Japan

## 1. Introduction

The depletion of fossil fuels necessitates alternative and sustainable energy sources for lasting human life.<sup>1</sup> Recently, electrochemical devices such as fuel cells (FCs) and battery systems, which can produce electricity from chemical reactions, have become a promising energy platform because of their highly efficient and convenient power generation techniques with eco-friendly process.<sup>1–5</sup> Significant efforts are underway towards developing new materials for each component in electrochemical devices, such as the anode, cathode, and electrolyte, to reduce the drawbacks or increase efficiency.<sup>5,6</sup>

In general, the performance of FCs is governed by the ion diffusion efficiency, where electrolyte and diffusing ions species

*Dae-Woon Lim is an Assistant Professor in the Department of Chemistry and Medical Chemistry, Yonsei University. He received his Ph.D. from Seoul National University (SNU) in Korea in 2014 under the supervision of Professor Myunghyun Paik Suh, after which, he moved to the Korea Atomic Energy Research Institute (KAERI) and Kyoto University as a postdoctoral fellow and Assistant Professor. His research interests cover the design of porous coordination polymers, nanocomposite materials for gas storage, catalysts, and ion/electron conductivity.*

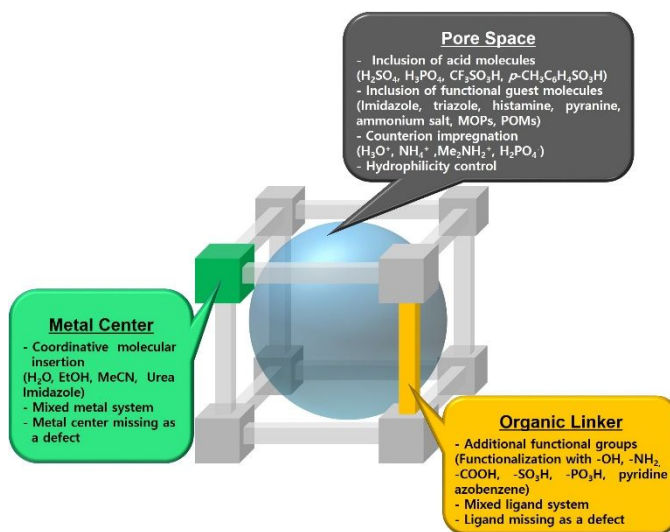


Fig 1. Strategies for proton conductive MOFs depending on the MOF components.

play a major role.<sup>7,8</sup> Compared with other ionic species such as Li<sup>+</sup> and Na<sup>+</sup>, the proton (H<sup>+</sup>) has exceptionally high mobility ( $36.2 \times 10^{-8} \text{ m}^2 \text{ s}^{-1} \text{ V}^{-1}$ ) in H<sub>2</sub>O,<sup>9</sup> and solid-state proton conductors show high conductivity due to the proton transport through the partial covalent nature of hydrogen bond (H-bond) with the reduced net charge in electrostatic interaction. Moreover, the solid-state electrolyte avoids the chronic safety issue caused by the leakage of liquid electrolyte. Initially, in 1950, Rogers and Ubbelohde suggested the occurrence of proton diffusion in solid-state acid sulphates of sodium, potassium, and ammonium,<sup>10</sup> where phase transition and H-bond based on the acid-base chemistry are important. Recently, the organic polymer-based electrolyte-like Nafion,<sup>11</sup> which works at a mild

temperature range ( $< 100\text{ }^{\circ}\text{C}$ ), is commercially available as a solid-state proton conductor and inorganic materials such as metal oxide and  $\text{CsHSO}_4$ <sup>12–14</sup> are studied as a proton conductor at a relatively high-temperature ( $> 100\text{ }^{\circ}\text{C}$ ). Although the conventional Nafions show high performance with  $\text{H}_2\text{O}$  conducting media, the efficiency degradation during the cyclic hydration and dehydration process and the high price of the material are the drawbacks. Therefore, the development of alternative materials is required. Most solid-state proton conductors demand a conducting medium as a part of the structure or guests to donate or carry the proton, which is strongly related to the possible fuel cell operating temperature. For instance,  $\text{H}_2\text{O}$  acts as an excellent conducting medium at a relatively mild temperature ( $< 85\text{ }^{\circ}\text{C}$ ) because of its low boiling point.<sup>15–17</sup> By contrast, non-volatile acids ( $\text{H}_2\text{SO}_4$ ,  $\text{H}_3\text{PO}_4$ )<sup>18–20</sup> or functional molecules such as imidazole,<sup>21,22</sup> triazole,<sup>23</sup> and ionic media<sup>24–26</sup> are able to work at high temperature ( $> 100\text{ }^{\circ}\text{C}$ ) even under anhydrous conditions. In addition to the conducting medium, the phase transition of a solid-state electrolyte induced by environmental conditions such as humidity<sup>27,28</sup>, temperature<sup>29</sup>, and pressure<sup>30</sup> can affect transport properties because of changes in the conducting pathway.

Most recently, porous crystalline metal-organic frameworks (MOFs) and porous coordination polymers (PCPs), constructed by metal ions and organic linkers, have received much attention as a new class of solid-state proton conductors.<sup>17,31–37</sup> MOFs are tuneable solids modulated by a limitless number of combinations of metal ions and organic ligands and have unique properties such as high porosity with a large surface area.<sup>38–40</sup> In particular, the tuneability and functionality of MOFs provide an opportunity to replace the conventional materials. According to the Cambridge Structural Database (CSD), the number of MOF structures estimated until 2017 was 70,000.<sup>41</sup> Since their development, MOFs have been extensively studied as a platform for various applications<sup>42,43</sup> such as gas storage<sup>44–47</sup>,  $\text{CO}_2$  capture and separation,<sup>48–54</sup> hydrocarbon separation,<sup>55,56</sup> isotope separation,<sup>57,58</sup> drug delivery,<sup>59,60</sup> catalyst,<sup>61,62</sup> nanoparticles fabrications,<sup>63–66</sup> sensor,<sup>67–70</sup> and supercapacitors.<sup>71</sup> Thus, the structural design and functionality

*Prof. Hiroshi Kitagawa was born in 1961 in Osaka; he finished his Ph.D. at Kyoto University in 1991, after which he became Assistant Professor at IMS and JAIST. He was appointed as Associate Professor at the University of Tsukuba in 2000. He became Professor of Chemistry at Kyushu University in 2003 and moved to Kyoto University as a Professor in 2009. He is now President of Japan Society of Coordination Chemistry. He has published more than 425 original research papers dealing with solid-state chemistry, coordination chemistry, nanoscience, low dimensional electrons system, and molecule-based conducto-*



of MOFs have been considered for the application of interests.

Kanda first reported the proton conductive MOF in 1979 with bis(2-hydroxyethyl)dithiooxamido] copper(II).<sup>72</sup> Subsequently, Kitagawa and Nagao reported on the proton transport in copper dithiooxamidate ( $(\text{HOC}_2\text{H}_4)_2\text{dtoaCu}$ ) and its derivatives.<sup>73,74</sup> To date, this field is growing rapidly. MOFs are advantageous for proton conduction because (1) their large inner surface area and void space can incorporate proton carriers as guests; (2) the long-range order of the structure enables visualization of the conducting pathway and mechanism; (3) the control of conductivity at the molecular level is beneficial for designing a new proton conductor. Nonetheless, there are some challenges to solve; (1) the chemical and thermal structure stability under the oxidation and reduction processes; (2) the voltage loss between the cathode and anode by hydrogen fuel crossover through the pore in the FC configuration; (3) the grain boundaries between the microcrystals are considered detrimental for practical use in proton exchange membranes (PEMs). In addition, (4) the dependence on humidity still presents a challenge for good conducting efficiency. Despite these, there has recently been an upsurge in the preparation of new proton-conductive MOFs, using new approaches such as intelligent predesign methods<sup>75–79</sup> and post-synthetic modifications (PSMs).<sup>80–84</sup> For the predesign methods, the structural stability against the humidity, chemicals, and temperature is considered because most of the conducting media, such as  $\text{H}_2\text{O}$ ,  $\text{NH}_3$ , and nonvolatile acids ( $\text{H}_2\text{SO}_4$  and  $\text{H}_3\text{PO}_4$ ), are detrimental to coordination compounds, so that the selection of metal species and organic linkers is decisive. For example, the inertness, oxidation state, and oxophilicity of metal ions can affect structural stability.<sup>85,86</sup> Indeed, the length of ligand and Lewis basicity can be intuitive factors for ligand selection, affecting the void space and the metal-ligand bond strength in MOFs.<sup>87–90</sup> Moreover, the selection of the hydrophilic functional groups and the induced extra-functional group in a ligand, which are not coordinated with the metal centre, are beneficial for improving the proton diffusion and the mobile proton concentration, providing an efficient conducting pathway. In addition, the charged networks, accompanying with simultaneous inclusion of the counterions ( $[\text{NH}_2\text{Me}_2]^+$  or  $[\text{NH}_2\text{Et}_2]^+$ ) in the framework can be formed during the synthetic procedure using amide-type solvents, where the counterions play proton donor and carrier in MOFs.<sup>16,91–93</sup> Another approach for proton-conductive MOFs is PSMs. In general, PSMs can be classified into the modification of coordination species in the metal centre,<sup>80,82,94–97</sup> a change in the functional groups of the ligand through an organic reaction,<sup>83,98–101</sup> and the inclusion of functional molecules into the pore.<sup>22,23,102,103</sup> Among these, the encapsulation of functional molecules into the pore is the simplest way, indicating dramatic changes in material properties. Finally, the imperfect structure, in other words, structural defects, can be considered one of the manipulations for improving proton conduction. Defective MOFs are fabricated by both predesign and PSMs.<sup>104,105</sup> The induced defect in the frameworks by the missing metal centre or organic linkers facilitates proton conduction by creating a conduction pathway.<sup>106–108</sup>

The proton-conducting mechanism in MOFs is characterized by X-ray structure analysis with various spectroscopic tools such as impedance measurements, solid-state nuclear magnetic resonance (SS-NMR) spectroscopy, and quasi-elastic neutron scattering (QENS) because of the correlation of the different molecular dynamics (MDs) of the conducting media and conduction mechanism.<sup>109</sup> According to the fundamental theory, proton diffuses by the either the “Grotthuss” or “vehicle” mechanism. In the former one, the proton is hopping from one site to another through the H-bonding with sequential molecular rotational reorientation.<sup>110</sup> In the latter case, protonic species such as  $\text{H}_3\text{O}^+$  and  $\text{NH}_4^+$  migrate directly as a proton attached to a vehicle.<sup>111</sup> In general, these two mechanisms have distinctive activation energies ( $E_a$ , Grotthuss mechanism  $< 0.4$  eV and vehicle  $> 0.4$  eV), reflecting the formation and dissociation of the H-bond. Experimentally,  $E_a$  is evaluated by a temperature-dependent conductivity measurement with the fitting of the Arrhenius equation (1).

$$\sigma = (\sigma_0/T) \exp(-E_a/kT) \quad (1)$$

where  $\sigma$ ,  $E_a$ ,  $k$ , and  $T$  are conductivity, the activation energy, the Boltzmann constant, and temperature, respectively. Nevertheless, in a practical situation, some cases indicate an ambiguous  $E_a$  value around the borderline of the Grotthuss and vehicle mechanisms, where the overall environment of the conduction pathway should be characterized and cross-checked by spectroscopic tools for intuitive understanding. Therefore, the only suggestion for  $E_a$  value is too general to describe the complicated cooperative proton conduction mechanism in MOFs.

The conductivity is represented by equation (2).

$$\sigma = nZe\mu \quad (2)$$

where  $n$ ,  $Ze$ , and  $\mu$  are the charge carrier concentration, a charge of the ionic species, and mobility. As seen in equation (2), the conductivity is affected by the concentration of charge carrier and mobility, which suggests a direction towards high proton-conductive MOFs research. Therefore, most researchers have focused on increasing the concentration of mobile protons in MOFs through the introduction of the acidic moiety.

As a general technique, the proton conductivity of MOFs has been measured with a pelletized sample by a two-terminal (2-probe) contact method, in which the average conductivity value is estimated due to randomly oriented microcrystals. However, conductivity measurement using a single crystal can distinguish the grain-boundary-free anisotropic conductivity. Therefore, type of conductivity measurement is critical for understanding proton-conductive MOFs with additional information.

There are numerous topics and issues that we could deal with in regard to the topic of proton-conductive MOFs (e.g. experimental methods to study proton conductivity, characterization of molecular dynamics (MDs), computational studies, and proton conductivity depending on the type of MOFs). However, in this review, we mainly focus on strategies for achieving proton-conductive MOFs with representative examples of activity in the field during the last decade.

## 2. Humidity and proton conductivity in MOFs

In real-world applications, the change in material properties and degradation by the presence of  $\text{H}_2\text{O}$  cannot be ignored. In particular, proton conductivity is intimately correlated to humidity because  $\text{H}_2\text{O}$  molecules are both proton donors and proton carriers, including the efficient H-bond. Therefore, the common water-mediated proton conductors demand high humidity with mild temperature ( $< 85$  °C) conditions. Indeed, MOFs have a similar tendency, and there are numerous examples of humidity dependence in proton-conductive MOFs. In this section, selected proton-conductive MOFs with unique strategies under the hydration and anhydrous conditions are discussed.

### 2.1. Proton conductivity under hydration

As mentioned above, hydration increases mobile proton concentration and creates a proton-conduction pathway through the H-bond. However, it is difficult to prove the relationship between the structural proton-conducting pathway change and proton conductivity directly. In 2014, Sadakiyo et al. visualized the H-bond network change in a proton-conductive MOF,  $(\text{NH}_4)_2(\text{adp})[\text{Zn}_2(\text{ox})_3] \cdot n\text{H}_2\text{O}$ , through single-crystal X-ray structure analysis under different humidity conditions (Fig. 2).<sup>15</sup> In the initial study, they reported the synthesis and proton conductivity in an oxalate-based two-dimensional (2D) anionic MOF,  $(\text{NH}_4)_2(\text{adp})[\text{Zn}_2(\text{ox})_3] \cdot n\text{H}_2\text{O}$ .<sup>75</sup> They verified the single-crystal structure of the fully hydrated sample,  $(\text{NH}_4)_2(\text{adp})[\text{Zn}_2(\text{ox})_3] \cdot 3\text{H}_2\text{O}$ , and showed that humidity-dependent conductivity increased up to  $8 \times 10^{-3} \text{ S cm}^{-1}$  at 25 °C and 98% relative humidity (RH). The high proton conductivity of  $(\text{NH}_4)_2(\text{adp})[\text{Zn}_2(\text{ox})_3] \cdot 3\text{H}_2\text{O}$  is attributed to the H-bond among the  $\text{NH}_4^+$  counterions, adipic acid (adp) organic molecules and  $\text{H}_2\text{O}$  guest molecules. In particular, the high conductivity is strongly affected by the change in humidity conditions by increasing the number of adsorbed  $\text{H}_2\text{O}$  molecules. Three different levels of hydrated samples, which involve the  $3\text{H}_2\text{O}$  (tri-hydrate),  $2\text{H}_2\text{O}$  (di-hydrate), and anhydrous states, were

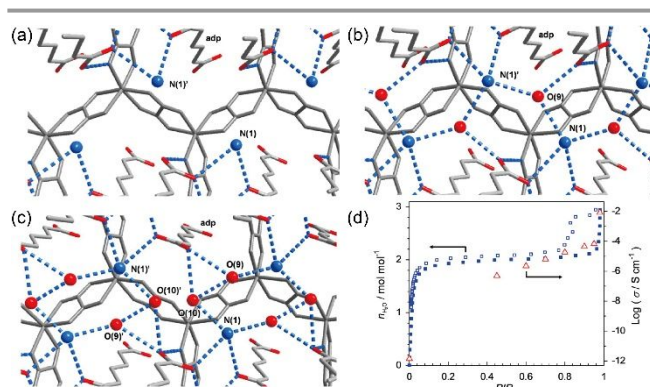


**Fig. 2.** Representation of hydrogen-bonding networks in (a)  $(\text{NH}_4)_2(\text{adp})[\text{Zn}_2(\text{ox})_3]$  (b)  $(\text{NH}_4)_2(\text{adp})[\text{Zn}_2(\text{ox})_3] \cdot 2\text{H}_2\text{O}$ . (c)  $(\text{NH}_4)_2(\text{adp})[\text{Zn}_2(\text{ox})_3] \cdot 3\text{H}_2\text{O}$ . (d) Proton conductivity and adsorption isotherms. Red triangles and blue squares correspond to proton conductivity (25 °C) and water vapor adsorption isotherms (25 °C), respectively.  $P/P_0$  corresponds to 100% RH. Reproduced from ref.15 with permission from the American Chemical Society, copyright 2014.

prepared. The tri-hydrated sample was an as-synthesized crystal, and the di-hydrated sample originated from the air-dried as-synthesized sample. According to the H<sub>2</sub>O vapor adsorption profile, (NH<sub>4</sub>)<sub>2</sub>(adp)[Zn<sub>2</sub>(ox)<sub>3</sub>] has two steps of adsorption profile with a small hysteresis and can be in the partially di-hydrated state in a wide humidity range (5% – 95% RH) (Fig. 2d). The anhydrous sample was prepared by drying the di-hydrated sample at 50 °C under N<sub>2</sub> flow. The structural transition between tri- and di-hydrated states is reversible at high humidity. During the phase transition, their space groups changed to tri-hydrate (*P*-1), di-hydrate (*P*<sub>2</sub><sub>1</sub>/*c*), and anhydrous (*P*<sub>2</sub><sub>1</sub>/*c*), respectively. The space group change is derived from the reorientation of adp molecules, which related to the slight hysteresis in H<sub>2</sub>O vapor sorption. Obviously, there is no significant structural change between the di-hydration and anhydrous states with the absence of hysteresis in H<sub>2</sub>O vapor sorption. The dehydration process indicates the reduced H-bond network among NH<sub>4</sub><sup>+</sup>, H<sub>2</sub>O, and adp (Fig. 2). In the di-hydrated sample, H<sub>2</sub>O and NH<sub>4</sub><sup>+</sup> are arranged alternatively in the interlayer space with simple H-bonding networks. Compared with the tri-hydrated state, the average H-bond distance in the di-hydrated state is longer, indicating a weakened H-bond network. In addition, the anhydrous state has a localized H-bond among NH<sub>4</sub><sup>+</sup>, ox, and adp because of the absence of guest H<sub>2</sub>O with a similar distance to those of the di-hydrate state. These distinctive H-bond network variations are directly reflected in the proton conductivity measured by alternating current (AC) impedance. The anhydrous sample has 10<sup>-12</sup> S cm<sup>-1</sup>, whereas the di- and tri-hydrate states have 7 × 10<sup>-5</sup> and 8 × 10<sup>-3</sup> S cm<sup>-1</sup>, respectively. This study directly represented the correlation of H<sub>2</sub>O adsorption with the structure of conducting pathways, resulting in proton conductivities.

The hydrophilicity of the host frameworks can control the hydration of MOFs. The hydrophilic MOFs have a strong affinity to water and can absorb large amounts of H<sub>2</sub>O molecules under the lower humidity condition, which improves proton conductivity even under ambient conditions. In 2012, Sadakiyo and coworkers reported the control of hydrophilicity in a bi-metallic oxalate-bridged layered compounds by incorporating counter cations with different lengths of alkyl chains (Fig. 3).<sup>77</sup> They prepared three compounds with the chemical formula, {NR<sub>3</sub>(CH<sub>2</sub>COOH)}[MCr(ox)<sub>3</sub>]*n*H<sub>2</sub>O, R-MCr, where R = Me (methyl), Et (ethyl), or Bu (*n*-butyl), and M = Mn or Fe. The honeycomb-based structures of [MCr(ox)<sub>3</sub>] have a 2D network, and the counter cations are aligned in the interlayer space with the carboxylic group locating in the honeycomb cavity. From the powder X-ray diffraction data (PXRD) fitting, the periodic interlayer distances of Bu-MnCr, Bu-FeCr, Et-MnCr, and Me-

FeCr was evaluated as 8.52, 8.49, 7.72, and 6.91 Å, respectively. According to the H<sub>2</sub>O vapor sorption, Me-FeCr and Et-MnCr show a larger uptake of H<sub>2</sub>O than does Bu-FeCr below 60% RH, implying a more hydrophilic interlayer space of Me-FeCr and Et-MnCr. The maximum uptake amounts at the highest humidity were 268, 134, and 57 cc g<sup>-1</sup> for Me-FeCr, Et-MnCr, and Bu-FeCr, respectively. The bulkiness of the alkyl chain reduced the hydrophilicity and void space in the frameworks simultaneously. As a result, Me-FeCr is a promising proton conductor under the low-humidity condition. To verify the conductivity, impedance spectroscopy was measured for pelletized Me-FeCr, Et-MnCr, Bu-FeCr, and Bu-MnCr. The conductivities at the low-humidity condition were 0.8 × 10<sup>-4</sup> (65% RH) for Me-FeCr, 1 × 10<sup>-7</sup> (65%) for Et-MnCr, 2 × 10<sup>-11</sup> (60%) for Bu-FeCr, and 0.8 × 10<sup>-11</sup> S cm<sup>-1</sup> (60%) for Bu-FeCr, respectively. The order of conductivity values coincides with the hydrophilicity and H<sub>2</sub>O uptake capacity for each compound, supporting that the hydrophilicity of MOFs triggers high proton conductivity under low humidity. Et-MnCr, Bu-FeCr, and Bu-FeCr indicated improved conductivities of 2 × 10<sup>-4</sup> (80% RH), 5 × 10<sup>-6</sup> (90% RH), and 0.9 × 10<sup>-7</sup> S cm<sup>-1</sup> (90% RH), respectively, at the limited maximum humidity because of the structural instability. Although the high conductivity under high humidity is promising, a relatively high conductivity under the ambient condition is more practical. This study provides that hydrophilicity can be a key to solving this problem.

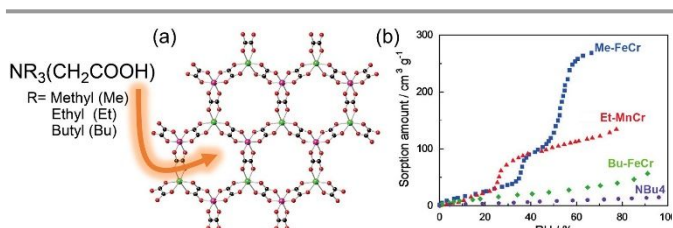


**Fig. 3.** (a) The crystal structure of {NR<sub>3</sub>(CH<sub>2</sub>COOH)}[MCr(ox)<sub>3</sub>]*n*H<sub>2</sub>O, where R = Me (methyl), Et (ethyl), or Bu (*n*-butyl), and M = Mn or Fe. (b) Water vapor adsorption isotherms of the MOFs at 298 K. Reproduced from ref.<sup>77</sup> with permission from the American Chemical Society, copyright 2012.

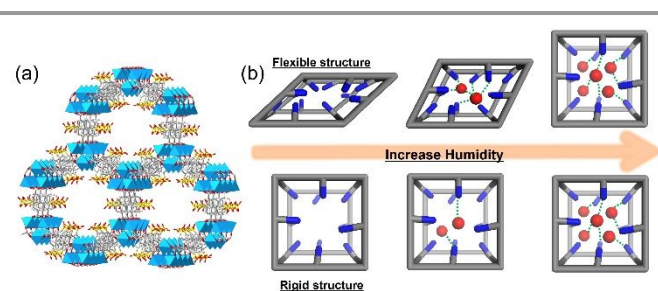


**Fig. 4.** (a) Structure of BUT-8(M) (M = Cr, Al). The M (M = Cr, Al), O, S, and C atoms are shown in blue polyhedral, red, yellow, and grey, respectively. (b) Proposed self-adaptation mechanism, where structural changes are induced by water adsorption in flexible MOFs; At low RH, the H-bonding networks in the pores are more uninterrupted in a flexible than in a rigid MOF.

The low conductivity under the low-humidity condition is attributed to the discontinuous (localized) H-bond network.<sup>15</sup> To avoid this problem, compared with rigid frameworks, the structural transformation response to the humidity level (self-adaptation) might be a new approach, where the flexible structure modifies the void space, maintaining a continuous H-bond network. In 2017, Yang and coworkers reported on the proton conductivity of a flexible Cr(II)-based MOF (BUT-8(Cr),  $\text{Cr}_3(\mu_3\text{-O})(\text{H}_2\text{O})_3(\text{NDC}(\text{SO}_3\text{H}_{5/6})_2)_3$ ;  $\text{NDC}(\text{SO}_3\text{H})_2$  = 4,8-disulfonaphthalene-2,6-dicarboxylate) with a highly decorated sulfonic acid site (Fig. 4).<sup>76</sup> The BUT-8 is a three-dimensional (3D) structure with a unidimensional (1D) channel along the *c*-axis, where the pore surface is decorated by sulfonic acid groups incorporating the  $(\text{CH}_3)_2(\text{NH}_2)^+$  cation because of the decomposition of the dimethylformamide (DMF) solvent. The counter cations are replaced by  $\text{H}^+$  (BUT-8 (Cr)A) through immersing the sample in  $\text{H}_2\text{SO}_4$  (0.5M). In PXRD, the broadened diffraction peaks of (BUT-8 (Cr)A) became sharp with humid air treatment. During vapor adsorption, the flexible MOF changes the unit cell parameter (*a*-axis) by 27.49% and overall cell volume by 37.58%, which is reflected in the PXRD peak shift to a lower angle. For comparison with proton conductivity in flexible MOFs and rigid structural MOFs (RMOFs), the AC impedance was measured for BUT-8(Cr), BUT-8(Cr)A, and MIL-101-SO<sub>3</sub> under the variable RH. The cation replaced BUT-8(Cr)A indicates a higher conductivity ( $6.35 \times 10^{-3} \text{ S cm}^{-1}$ ) compared with that of pristine BUT-8(Cr) ( $1.12 \times 10^{-3} \text{ S cm}^{-1}$ ) under the same condition (65% RH, 25 °C), whereas the RMOF (MIL-101-SO<sub>3</sub>) shows a conductivity of  $5.92 \times 10^{-4} \text{ S cm}^{-1}$  at 25 °C and 65% RH. Furthermore, BUT-8(Cr)A and BUT-8(Cr) exhibit moderate conductivities of  $4.19 \times 10^{-6}$  and  $5.75 \times 10^{-7} \text{ S cm}^{-1}$  at the lower RH of 11%, which are much higher than that of MIL-101-SO<sub>3</sub> ( $5.84 \times 10^{-9} \text{ S cm}^{-1}$ ). Under the maximum humidity (100%) at 25 °C, the conductivity of BUT-8(Cr)A and BUT-8(Cr) increased up to  $7.61 \times 10^{-2} \text{ S cm}^{-1}$  and  $1.50 \times 10^{-2} \text{ S cm}^{-1}$ , respectively. The electrical conductivities of both samples were  $5.10 \times 10^{-8}$  and  $1.28 \times 10^{-8} \text{ S cm}^{-1}$  under the same conditions, implying the proton conductor and electronic insulator. At the low-humidity level range (11%–65%), the conductivity of flexible MOFs did not have a linear correlation with the H<sub>2</sub>O content, while RMOF presented a straight linearity in the range. Unlike the rigid MOF, the unique water dependence of the proton conductivity in flexible MOFs might be attributed to their structural self-adaptation phenomenon. At high temperature and humidity (80 °C and 100% RH), the conductivities of MIL-101-SO<sub>3</sub>H, BUT-8(Cr)A, and BUT-8(Cr) were further improved up to  $1.16 \times 10^{-2}$ ,  $4.63 \times 10^{-2}$ , and  $1.27 \times 10^{-1} \text{ S cm}^{-1}$ , respectively. The activation energy ( $E_a$ ) values evaluated from the linear fitting by the Arrhenius equation for BUT-8(Cr)A, BUT-8(Cr), and MIL-101-SO<sub>3</sub>H are 0.11, 0.21, and 0.23 eV, respectively. These results rationalize the fast ion-diffusion by the Grotthuss mechanism. This study shows evidence that structural flexibility helps to maintain the relatively high proton conductivity by adapting external stimulus through the humidity-dependent structural transformation.

The humidity dependence of proton conductivity is a general strategy in solid-state proton conductors with a change

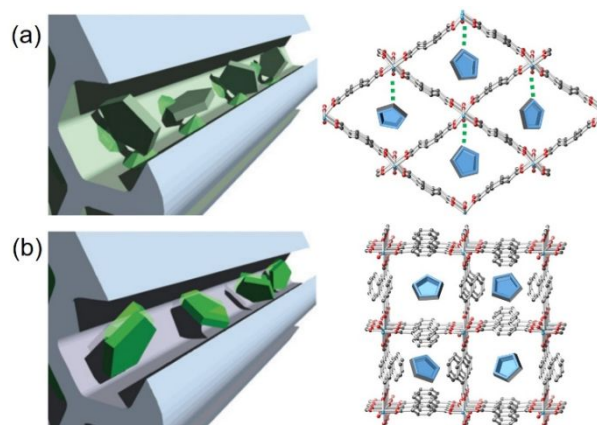


**Fig. 5.** (a) Im accommodated in a nanochannel containing the active site with high affinity to im (Im@2). The strong host-guest interaction retards the mobility of im to afford the low proton conductivity. (b) Im are accommodated in a nanochannel without strong host-guest interaction (Im@1) and therefore, the molecules obtain the high mobility to show high proton conductivity. Reproduced from ref.22 with permission from Nature Publishing Group, copyright 2009.

in H-bond networks. Thus, the increased affinity of frameworks to H<sub>2</sub>O for a strong H-bond is significant. In addition, a framework that responds to external stimuli such as humidity and temperature would be a promising candidate for advanced materials. Although there are numerous H<sub>2</sub>O-mediated proton-conductive MOFs, only selected examples are introduced in this section. More variable strategies are discussed in the manipulation of each component in MOFs.

## 2.2. Proton conductivity under the anhydrous condition

The proton conduction at intermediate temperature (100–200 °C) is a significant challenge in proton exchange membrane (PEM) and direct methanol fuel cell (DMFC), and has following advantages. (1) The kinetically faster reaction in the electrode is able to use cheaper catalysis.<sup>112</sup> (2) The waste heat can be recyclable.<sup>4</sup> (3) The high-temperature operation (> 150 °C) improves the efficiency with the reduction in CO poisoning in FCs.<sup>113,114</sup> Therefore, proton conductivity under the anhydrous condition is essential. In particular, the inherent proton conductivity is beneficial for high-temperature conductivity as the presence of H<sub>2</sub>O molecules becomes unnecessary. The key factors for attaining the intrinsic proton conduction are charge carrier concentration, acidity, and structure. In addition, instead of water molecules, alternative non-volatile conducting media with high boiling points, such as imidazole (Im) and triazole, and a strong H-bonding interaction between the chemical components in the framework are required.

Anhydrous proton conductive MOFs were initially reported by Bureekaew and co-workers in 2009.<sup>22</sup> They used Al-based MOFs ( $[\text{Al}(\mu_2\text{-OH})(1,4\text{-ndc})]_n$  (**1**; 1,4-ndc: 1,4-naphthalenedicarboxylate) and  $[\text{Al}(\mu_2\text{-OH})(1,4\text{-bdc})]_n$  (**2**; 1,4-bdc: 1,4-benzenedicarboxylate) with incorporation of Im molecules in the pore to understand the correlation of Im mobility with conductivity. In this study, the molecular mobility of conducting media in confined space with different environment is a key for high proton conductivity (Fig. 5). Both

Al-based MOFs have a 1D metal chain bridged by  $\text{-OH}$ , showing a 1D pore structure with a dimension of about 8 Å. However, the pore shape, surface potential, and incorporated Im contents are different (Fig. 5). Thus, the principal difference between two compounds originated from the 1,4-ndc and 1,4-bdc ligands. The additional benzene ring of naphthalene ligand in compound **1** exposes to the pore direction, inducing steric hindrance with interruption of the interaction between the guest Im molecules and the  $\mu_2\text{-OH}$  bridging ligand/carboxylate around the metal centre. By contrast, compound **2** has a single benzene ring, where the polar sites protrude in the pore direction, aiding the host-guest interaction. The difference in affinity of the host-guest interaction retards the mobility of guest molecules, resulting in the low conductivity. The accommodated Im contents in compounds **1** and **2** were 0.6 (Im)/Al ion (14 wt%) and 1.3 (Im)/Al ion (30 wt%), respectively. The Im in compound **1** is released by heating in a single step in the range of 160–225 °C, while compound **2** emits Im in two steps (130–160 and 160–240 °C), indicating the different host-guest interaction. The conductivity was measured by AC impedance spectroscopy under  $\text{N}_2$  atmosphere below 130 °C before the loss of Im molecules. Bulk-state Im has a low conductivity ( $\sim 10^{-8} \text{ S cm}^{-1}$ ) at ambient temperature<sup>115</sup> and the conductivity for the guest-free form of compound **1** is  $10^{-13} \text{ S cm}^{-1}$ . However, the conductivity progresses to  $5.5 \times 10^{-8} \text{ S cm}^{-1}$  at room temperature (RT) after incorporation of Im. Subsequently, as the temperature increased to 120 °C, the conductivity significantly improved to  $2.2 \times 10^{-5} \text{ S cm}^{-1}$  with  $E_a$  of 0.6 eV. As mentioned above, a higher carrier concentration can improve conductivity in general. Nonetheless, compound **2** indicates a lower conductivity of  $\sim 10^{-10} \text{ S cm}^{-1}$  at RT and  $1 \times 10^{-7} \text{ S cm}^{-1}$  at 120 °C with  $E_a$  of 0.9 eV. The conductivity decreased by two orders of magnitude, which is attributed to the strong interaction between the polar Im molecules and the polar pore surface. The molecular dynamics (MDs) of Im, measured by temperature-dependent  $^2\text{H}$  SS-NMR supports that the isotropic signal by thermal activation of Im@**1** starts to appear at 20 °C between the Pake-type double pattern, and the only isotropic signal exists at 80 °C. In contrast, Im@Compound **2** indicates an anisotropic signal (Pake-type double pattern) over the whole temperature range, which means that Im in compound **1** is much more mobile than that in compound **2**. Consequently, it is concluded that the degree of charge-carrier mobility in the confined spaces is strongly correlated to the conductivity.

In 2009, Hurd and co-workers reported on the anhydrous proton conductivity at 150 °C in Na-based sulfonate frameworks ( $\text{Na}_3(2,4,6\text{-trihydroxy-1,3,5-benzenetrisulfonate})$ ,  $\beta\text{-PCMOF2}$ ) by the loading of amphoteric triazole molecules (Tz, 1H-1,2,4-triazole).<sup>23</sup> The Na-based sulfonate framework has two phases, a low-temperature  $\alpha$ -phase and a high-temperature  $\beta$ -phase, exhibiting a honeycomb structure with a 1D pore. The pore consists of oxygen atoms of the sulfonate group. First, the conductivity of the pristine sample,  $\beta\text{-PCMOF2}(\text{H}_2\text{O})_{0.5}$ , is  $5.0 \times 10^{-6} \text{ S cm}^{-1}$  at 30 °C, and it drops down below  $10^{-7} \text{ S cm}^{-1}$  above 70 °C due to dehydration. The guest  $\text{H}_2\text{O}$  molecules are replaced by an amphoteric N-heterocycle (1H-1,2,4-triazole (Tz)) for high-temperature proton conductivity through *in situ* Tz loading

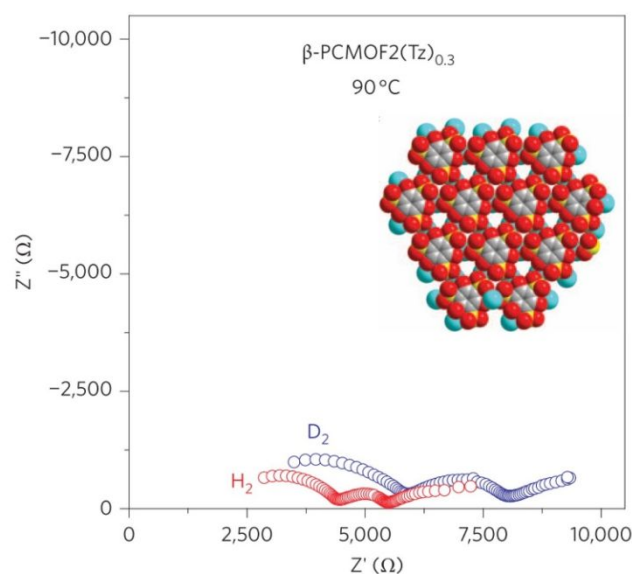


Fig. 6. AC impedance plots of as-pressed pellets of  $\beta\text{-PCMOF2}(\text{Tz})_{0.3}$  at 90 °C in dry  $\text{H}_2$  and  $\text{D}_2$ . Inset: Structure of  $\beta\text{-PCMOF2}$  with a space-filling diagram down the axis of the pores. Reproduced from ref.23 with permission from Nature Publishing Group, copyright 2009.

into the  $\alpha$ -phase and sequential conversion to the  $\beta$ -phase with heating. The overall structural change does not happen, and free Tz molecules are not observed. The controlled loading amounts ( $x$ ) of Tz in  $\beta\text{-PCMOF2}(\text{Tz})_x$  were  $x = 0.3, 0.45, \text{ and } 0.6$ . At 150 °C, the conductivities of  $\beta\text{-PCMOF2}(\text{Tz})_{x=0.3, 0.45, 0.6}$  show  $2 \times 10^{-4}$  ( $x = 0.3$ ),  $5 \times 10^{-4}$  ( $x = 0.45$ ), and  $4 \times 10^{-4} \text{ S cm}^{-1}$  ( $x = 0.6$ ), respectively, despite low conductivity ( $< 10^{-6} \text{ S cm}^{-1}$ ) for pure Tz and  $\beta\text{-PCMOF2}$ . To determine the conductivity by proton conduction rather than electron or  $\text{Na}^+$ , the AC impedance was measured in  $\beta\text{-PCMOF2}(\text{Tz})_{0.3}$  using  $\text{H}_2$  and  $\text{D}_2$  gas diffusion electrodes. The impedance plot represents three clear semicircles derived from bulk, grain boundary, and electrode polarization. Furthermore,  $\text{H}_2$  has a higher conductivity than  $\text{D}_2$  by a factor of  $\sim 1.5$  times due to the kinetic isotope effect (Fig. 6). The activation energy depends on the Tz loading amounts in  $\beta\text{-PCMOF2}(\text{Tz})_x$ .  $\beta\text{-PCMOF2}(\text{Tz})_{0.3}$  has a single slope with 0.51 eV in the range of 23–150 °C. By contrast,  $x = 0.45$  and 0.6 have a change in slope with two activation energies ( $x = 0.45$ ; 1.8 eV in the range of 50–90 °C and 0.34 eV for 90–150 °C;  $x = 0.6$ ; 1.87 eV in the range of 23–80 °C and 0.56 eV for 80–150 °C). Further confirmation for potential application of the membrane was performed using a membrane-electrode assembly (MEA). The open-circuit voltage (OCV) was 1.18 V for 72 h at 100 °C and subsequently, decreased to 0.93 and 0.77 V at 120 and 140 °C because of the fuel crossover. This study almost first shows a design for high-temperature proton conductivity in MOF.

The anhydrous proton conductivity of the “plastic crystal”, phosphate-type coordination polymer, was reported in 2012 by Horike and co-workers.<sup>116</sup> The conventional plastic crystals are classified into molecular and ionic crystals, where molecules or ions are discrete. Although the ionic crystal is considered to be a promising candidate for ionic conductors, there is a synthetic limitation, having a weak Coulombic interaction. The phosphate-type MOF is constructed by protonated Im and an

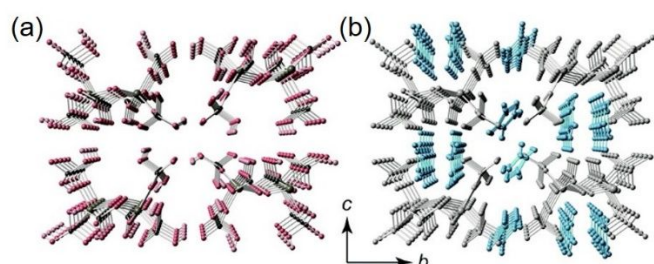


Fig. 7. (a) Packing structure of four  $[\text{Zn}(\text{HPO}_4)(\text{H}_2\text{PO}_4)_2]^{2-}$  chains along the  $a$ -axis. Zn, P, O, and H atoms are grey, black, red, and pink, respectively. (b) Crystal structure of  $[\text{Zn}(\text{HPO}_4)(\text{H}_2\text{PO}_4)_2](\text{ImH}_2)_2$ . The  $\text{ImH}_2^+$  ions are highlighted in blue and the networks are grey. H atoms in the networks have been omitted. Reproduced from ref.116 with permission from the American Chemical Society, Copyright 2012.

anionic 1D chain of  $\text{Zn}^{2+}$ -phosphate,  $[\text{Zn}(\text{HPO}_4)(\text{H}_2\text{PO}_4)_2](\text{ImH}_2)_2$  (Fig. 7).  $\text{Zn}^{2+}$  has tetrahedral coordination, and two types of orthophosphates are present, resulting in a 1D chain along the  $a$ -axis with  $-2$  charge. To compensate for the negative charge, two crystallographically independent protonated Ims are observed between the chains. The close-packed  $\text{ImH}_2^+$  molecules and negatively charged Zn chain have a potential interionic proton hopping pathway.  $[\text{Zn}(\text{HPO}_4)(\text{H}_2\text{PO}_4)_2](\text{ImH}_2)_2$  does not show any weight loss up to  $200^\circ\text{C}$ , and the PXRD pattern is the same at  $30^\circ\text{C}$  and  $140^\circ\text{C}$ . Therefore, anhydrous conductivity was measured from  $25^\circ\text{C}$  and  $130^\circ\text{C}$ . At  $25^\circ\text{C}$ , the proton conductivity of  $[\text{Zn}(\text{HPO}_4)(\text{H}_2\text{PO}_4)_2](\text{ImH}_2)_2$  is  $3.3 \times 10^{-8} \text{ S cm}^{-1}$ , and a steep jump is observed around  $55^\circ\text{C}$ . Finally, the conductivity reaches  $2.3 \times 10^{-4} \text{ S cm}^{-1}$  at  $130^\circ\text{C}$  and remains at this level for 12 h. The steep increase in conductivity around  $55^\circ\text{C}$  is thought to be a change in motion of the mobile ion that is a behaviour of plastic crystals. This phenomenon can be proved by the differential scanning calorimetry (DSC) profile. The single-crystal X-ray analysis at  $70^\circ\text{C}$  exhibits the heavily disordered one of two  $\text{ImH}_2^+$  compared with the structure at  $-30^\circ\text{C}$ . The evaluated  $E_a$  between  $130$  and  $40^\circ\text{C}$  is  $0.47 \text{ eV}$ , and the Grotthuss mechanism contributes mainly. The OCV using MEA ( $\text{H}_2/\text{air}$  cell) is  $0.75 \text{ V}$  at  $150^\circ\text{C}$  for 1 h. Although there is no weight loss up to  $200^\circ\text{C}$ , endothermic peaks are observed at  $70^\circ\text{C}$  and  $160^\circ\text{C}$ , which is the melting point. The melting occurs in the range of  $70$ – $160^\circ\text{C}$ , and there are no XRD peaks after cooling. However, the crystallinity is recovered by a physical stimulus, like a scratch. Its conductivity is  $2.0 \times 10^{-4} \text{ S cm}^{-1}$  at  $130^\circ\text{C}$ , similar to the original state. This work emphasized the importance of short-range disorder in a long-range ordered crystal for intrinsic proton conductivity by phase transition.

Nagakar and co-workers reported a rigid proton-conductive MOF,  $[(\text{Me}_2\text{NH}_2)_3(\text{SO}_4)_2]_2[\text{Zn}_2(\text{ox})_3]_n$ ,<sup>117</sup> which works under the hydration and anhydrous conditions (Fig. 8).<sup>118</sup> To design a proton conductive MOF, they screened for a potential candidate in the CSD, which meets the criteria for the presence of high-boiling proton carriers, high carrier concentration, and the extent of H-bonding. In  $[(\text{Me}_2\text{NH}_2)_3(\text{SO}_4)_2]_2[\text{Zn}_2(\text{ox})_3]_n$ , the  $[\text{Zn}_2(\text{ox})_3]^{2-}$ , the anionic framework interpenetrates the cationic supramolecular net  $[(\text{Me}_2\text{NH}_2)_3\text{SO}_4]^+$ , which has electrostatic interaction and H-bond networks between the sulfate anion and dimethylammonium  $(\text{Me}_2\text{NH}_2)^+$ . The overall structure is

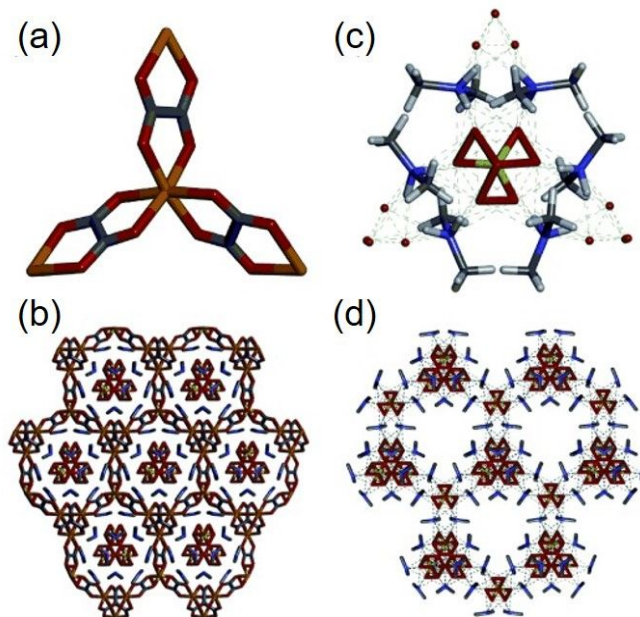
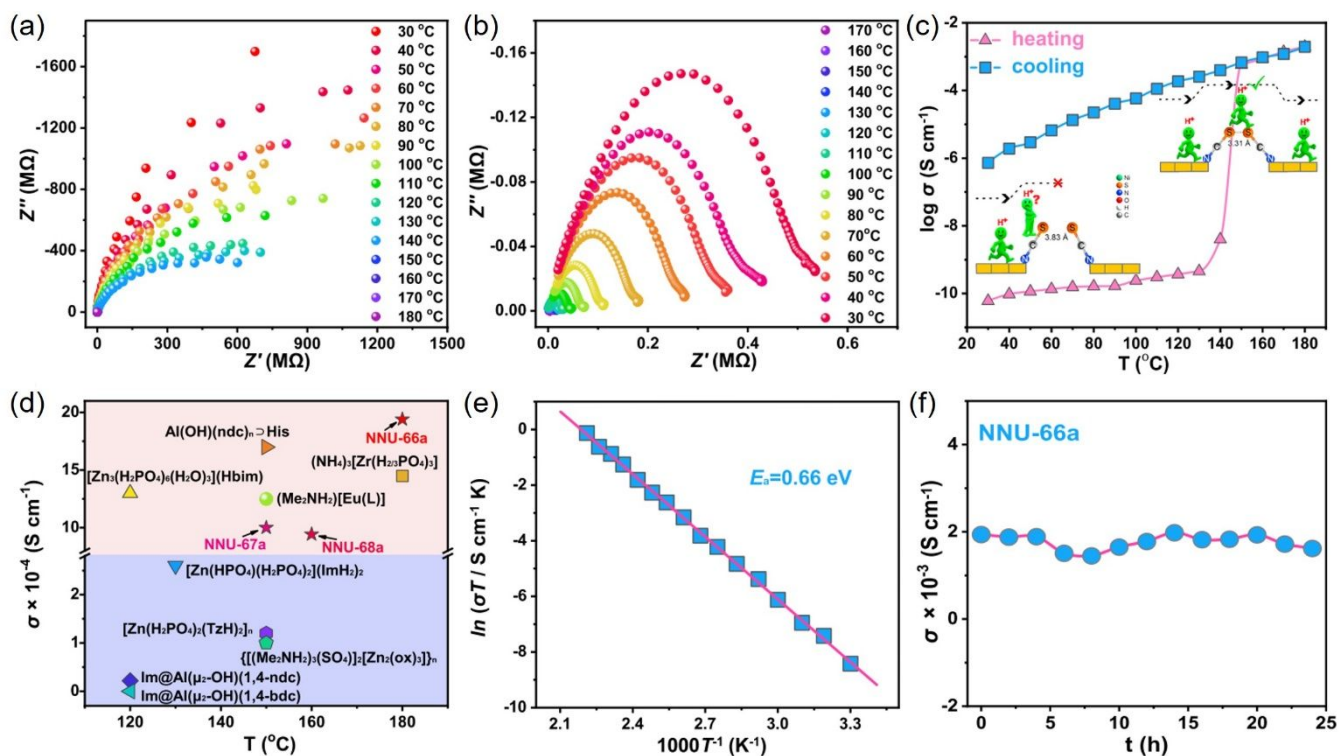


Fig. 8. (a) The tris-chelated  $D_3$ -symmetric  $[\text{Zn}_2(\text{ox})_3]^{2-}$  subunit. (b) Crystal structure of  $\{[(\text{Me}_2\text{NH}_2)_3(\text{SO}_4)_2][\text{Zn}_2(\text{ox})_3]\}_n$ . (c) Hydrogen-bonding interactions between dimethyl ammonium cations and sulfate anions. (d) 3D supramolecular  $[(\text{Me}_2\text{NH}_2)_3\text{SO}_4]^+$  net formed by hydrogen bonding between dimethyl ammonium cations and sulfate anions. C grey, N blue, O red, S yellow, Zn orange. Reproduced from ref.117 with permission from 2014 Wiley-VCH.

thermally stable up to  $180^\circ\text{C}$ . It does not show porosity on  $\text{N}_2$  sorption at  $77 \text{ K}$ . Nevertheless, the  $\text{H}_2\text{O}$  adsorption capacity is about 5 wt%. The H-bond signal reveals strong and broad peaks in infrared (IR) spectroscopy at  $3400$ – $3500$  and  $2780 \text{ cm}^{-1}$  for the N–H stretching vibration and a sharp peak at  $1000$ – $1300 \text{ cm}^{-1}$  for sulfate. The proton conductivity expected by the H-bond network was measured by AC impedance spectroscopy under anhydrous conditions. At  $30^\circ\text{C}$ , the conductivity was  $7 \times 10^{-5} \text{ S cm}^{-1}$  and improved to  $1 \times 10^{-4} \text{ S cm}^{-1}$  at  $150^\circ\text{C}$  with  $E_a$  of  $0.129 \text{ eV}$ , assuming the Grotthuss mechanism. The origin of high proton conductivity under the anhydrous condition is attributed to the H-bond in the supramolecular interaction in  $[(\text{Me}_2\text{NH}_2)_3(\text{SO}_4)]^+$  rather than to other ionic species or phase transition. The  $\text{H}_2\text{O}$  effect in conductivity was measured with different humidity levels. At 30% RH and RT, the conductivity was  $4.4 \times 10^{-5} \text{ S cm}^{-1}$ , and reached  $4.2 \times 10^{-2} \text{ S cm}^{-1}$  at 98% RH. Furthermore,  $\text{D}_2\text{O}$ -mediated conductivity was measured to verify the isotope effect in conductivity, resulting in a slightly low conductivity of  $3.7 \times 10^{-2} \text{ S cm}^{-1}$ . The high proton conductivity in  $\text{H}_2\text{O}$ -mediated conditions is thought to be due to an acid–base pair caused by a dissociative proton in  $\text{Me}_2\text{NH}_2^+$  in water. Unlike other proton-conductive MOFs, this compound indicates a high proton-conducting property in both humidifying and anhydrous conditions.

Most recently, Li and co-workers reported a high proton conductivity at  $180^\circ\text{C}$  with a hysteresis phenomenon in Ni, Fe, and Co-based trinuclear cluster by structural transformation.<sup>119</sup> In fact, these complexes cannot be classified into MOFs. However, the strategy for anhydrous proton conductivity is applicable in MOF chemistry. The three trinuclear clusters,  $[\text{Ni}_3(\text{NH}_2\text{-trz})_6(\text{SCN})_4(\text{H}_2\text{O})_2][\text{SCN}]_2 \cdot \text{H}_2\text{O}$  (NNU-66,  $\text{NH}_2\text{-trz} = 4$ –

amino-1,2,4-triazole), and its isomeric [Fe<sub>3</sub>(NH<sub>2</sub>- and two coordinated SCN<sup>-</sup> anions, resulting in an octahedral



trz)<sub>6</sub>(SCN)<sub>4</sub>(H<sub>2</sub>O)<sub>2</sub>](SCN)<sub>2</sub>·H<sub>2</sub>O (NNU-67) and [Co<sub>3</sub>(NH<sub>2</sub>-trz)<sub>6</sub>(SCN)<sub>4</sub>(H<sub>2</sub>O)<sub>2</sub>](SCN)<sub>2</sub>·H<sub>2</sub>O (NNU-68), were synthesized in a solvothermal reaction. These complexes have an identical structure with different metal species. The central metal is coordinated by six-NH<sub>2</sub>-trz bridging ligands. Each terminal metal on both sides has three-NH<sub>2</sub>-trz ligands, one coordinated H<sub>2</sub>O,

geometry configuration. In addition, one lattice H<sub>2</sub>O and two free SCN<sup>-</sup> anions are present in the overall framework. In the temperature range of 150-180 °C, NNU-66 shows a phase transition by rearrangement of the trinuclear cluster and change of free anions and H<sub>2</sub>O molecules without composition

**Fig. 9.** Proton conductivity (a and b) Nyquist plots of NNU-66 and NNU-66a at temperature ranges of (a) 30–180 °C and (b) 170–30 °C. (c) Temperature-dependent proton conductivities of NNU-66 and NNU-66a (30–180 °C). (d) Comparison of the proton conductivity among NNU-66a, NNU-67a, NNU-68a, and some other representative materials. (e) Arrhenius plot of NNU-66a in the temperature range of 30–180 °C. (f) Time-dependent proton conductivity of NNU-66a performed at 180–150 °C. Reproduced from ref.119 with permission from Cell Press, copyright 2020.

change (NNU-66a), which was analysed by single-crystal X-ray analysis. For anhydrous proton conductivity measurements, the upper temperature limit for three complexes is determined by thermal structure stability (NNU-66 = 180 °C, NNU-67 = 150 °C, and NNU-68 = 160 °C). The proton conductivity of three complexes suddenly increases as the temperature increases (NNU-66: from 3.98 × 10<sup>-9</sup> S cm<sup>-1</sup> at 140 °C to 5.8 × 10<sup>-4</sup> S cm<sup>-1</sup> at 150 °C, NNU-67: from 1.59 × 10<sup>-7</sup> S cm<sup>-1</sup> at 130 °C to 4.47 × 10<sup>-4</sup> S cm<sup>-1</sup> at 140 °C, NNU-68: 3.90 × 10<sup>-8</sup> S cm<sup>-1</sup> at 150 °C to 9.43 × 10<sup>-4</sup> S cm<sup>-1</sup> at 160 °C). At the upper temperature limit, the structural transformation of NNU-66a and NNU-67a reached conductivities of 1.94 × 10<sup>-3</sup> (E<sub>a</sub> = 0.66 eV) and 1 × 10<sup>-3</sup> S cm<sup>-1</sup> (E<sub>a</sub> = 0.71 eV) at 180 °C and 150, respectively (Fig. 9). The activation energy values suggest a dominant vehicle mechanism of proton diffusion using the free H<sub>2</sub>O and SCN<sup>-</sup> anions as proton carriers. Based on the single-crystal X-ray structure analysis of the heated form, the effective zigzag arrangement of SCN<sup>-</sup> was observed, where SCN<sup>-</sup> anions make a “bridge” with adjacent SCN<sup>-</sup>. Meanwhile, the low-temperature state has a long distance between SCN<sup>-</sup> molecules with inefficient proton

transport. From the density functional theory (DFT) calculation based on X-ray structure, the required energy for proton hopping between the adjacent SCN<sup>-</sup> with a distance of 3.83 Å is 0.34 eV. However, the heated form of NNU-66a has a shorter length, indicating that a negligible energy is required. Therefore, the structural transformation can create an efficient conducting pathway that is superficially invisible, indicating high proton conductivity.

In contrast to hydration condition, the anhydrous proton-conductive MOFs reported until show the highest conductivity of ~10<sup>-3</sup> S cm<sup>-1</sup>. Although the maximum conductivity reported is not a fundamental limit, the key to overcoming this limitation is that the H-bond network should not be destructive or transform more efficiently as the temperature rises. Therefore, the designing of possible frameworks and conducting media for comparable conductivity to H<sub>2</sub>O could be a future endeavour.

### 3. Various strategies for proton-conductive MOFs

#### 3.1 Strategies for manipulating the metal component

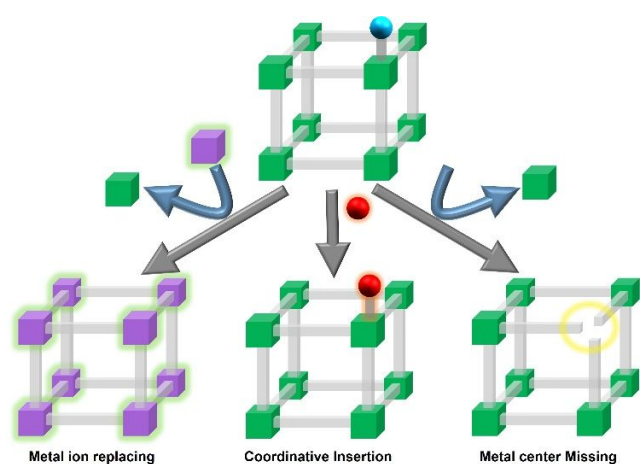


**Fig 10.** Schematic illustration of the manipulating strategies for the metal component.

Based on the coordination chemistry, the coordination number and geometry of metal ions in MOFs are essential factors for the structural design and stability of MOFs. In particular, tuning of the inorganic clusters in MOFs through metal exchange or mixed-valence with redox reaction can affect the physical and electronic properties of MOFs.<sup>120–123</sup> In addition, metal clusters sometimes include the coordinated solvent during the synthetic process, which can be removed by activation processes such as heating/vacuum or supercritical CO<sub>2</sub> drying, generating vacant coordination site called “open metal sites” (OMSs).<sup>124</sup> These OMSs provide the active site to interact with guest molecules for an adsorption catalytic reaction.<sup>125</sup> Furthermore, the replacement of coordination solvents with functional organic molecules induces the pore surface decoration and pore size control in MOFs. For proton-conductive MOFs, there are three representative strategies of metal unit manipulations, namely (1) metal ion replacing (2) the coordinative insert of functional organic molecules in OMSs (3) the metal-centre missing as a defect site (Fig. 10).

#### Metal centre exchange and coordinative insertion

In 2020, Liu and co-workers reported on the improved proton conductivity in Fe-MIL-88B through the replacement of the metal ion to Cr<sup>3+</sup> and subsequently coordinative insertion of 3-pyridinesulfonic acid (PSA) and 2-(4-pyridyl) ethanesulfonic acid (PESA) (Fig 11).<sup>126</sup> Fe-MIL-88B [Fe<sub>3</sub>O(bdc)<sub>3</sub>]<sub>x</sub>, x = coordinated molecules in OMS], is constructed by the Fe (III) trimer and 1,4-benzendicarboxylic acid, indicating a hexagonal channel (15.6 Å) along the *c*-axis with a coordinate solvent in the metal centre.<sup>127</sup> Although Fe-MIL-88B is advantageous due

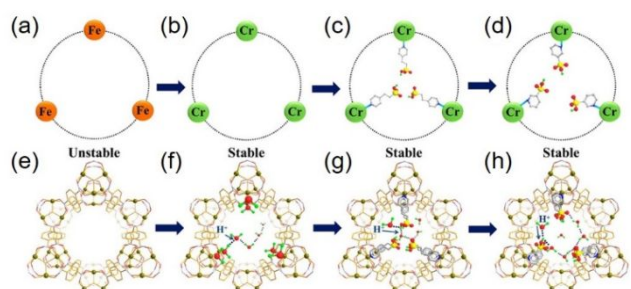


**Fig 11.** Schematic open channels with metal atoms of the MIL-88B structure: (a, b, c, d) unstable Fe-MIL-88B, stable Cr-MIL-88B, Cr-MIL-88B-PESA, and Cr-MIL-88B-PSA. (e, f, g, h) Structures of Fe-MIL-88B, Cr-MIL-88B, Cr-MIL-88B-PESA, and Cr-MIL-88B-PSA viewed along the *c*-axis, and the evolution of stability and proton conductivity. Colour code: O, red; C, grey; N, blue; S, yellow; H, light green; Cr, dark gold. Reproduced from ref.127 with permission from the American Chemical Society, copyright 2020

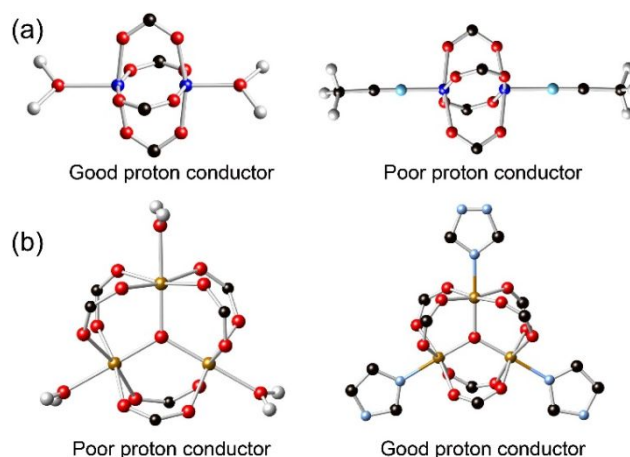


**Fig 12.** Coordinative insertion of OMSs of amphoteric molecules in a Cu-paddle (from ref.82) and Fe<sup>III</sup><sub>2</sub>Fe<sup>II</sup>(μ<sub>3</sub>-O) cluster (from ref.128).

to the high porosity with the potential OMSs, its weak structural stability is a drawback for a proton-conductive MOF. Therefore, replacing the metal centre with inert species is a good approach for enhanced structural stability. The metal species and the coordinated functional organic molecules are controlled in the synthetic step, resulting in Cr-MIL-88B [Cr<sub>6</sub>O<sub>2</sub>F<sub>2</sub>(C<sub>8</sub>O<sub>4</sub>H<sub>4</sub>)<sub>6</sub>](C<sub>3</sub>H<sub>7</sub>NO)<sub>2.80</sub>, Cr-MIL-88B-PESA [Cr<sub>6</sub>O<sub>2</sub>F<sub>2</sub>(C<sub>8</sub>O<sub>4</sub>H<sub>4</sub>)<sub>6</sub>(C<sub>7</sub>H<sub>9</sub>NO<sub>3</sub>S)<sub>1.45</sub>](C<sub>3</sub>H<sub>7</sub>NO)<sub>5.6</sub>, and Cr-MIL-88B-PSA [Cr<sub>6</sub>O<sub>2</sub>F<sub>2</sub>(C<sub>8</sub>O<sub>4</sub>H<sub>4</sub>)<sub>6</sub>(C<sub>5</sub>H<sub>5</sub>NO<sub>3</sub>S)<sub>1.52</sub>](C<sub>3</sub>H<sub>7</sub>NO)<sub>5.5</sub>. These samples have high thermal stability up to 350–400 °C. In the H<sub>2</sub>O vapor sorption at 25 °C, three samples adsorbed H<sub>2</sub>O of 21.26 mol/mol for Cr-MIL-88B, 39.81 mol/mol for Cr-MIL-88B-PESA, and 30.74 mol/mol for Cr-MIL-88B-PSA with a different slope, implying a strong affinity of sulfonic acid-decorated samples. The AC impedance was measured with pelletized samples under varying humidity and temperature. At 85% RH and 100 °C, Cr-MIL-88B shows a conductivity value of 6 × 10<sup>-3</sup> S cm<sup>-1</sup>, whereas MIL-88B-PESA and Cr-MIL-88B-PSA have conductivity values of 4.50 × 10<sup>-2</sup> and 1.58 × 10<sup>-1</sup> S cm<sup>-1</sup>, respectively. The slight difference in conductivity of MIL-88B-PESA and Cr-MIL-88B-PSA originated from the number of SO<sub>3</sub>H and pK<sub>a</sub> (pK<sub>a\_PESA</sub> = 5.68 and pK<sub>a\_PSA</sub> = 3.12). The conduction mechanism evaluated from the temperature dependent conductivities is vehicular diffusion at RH < 68% and Grotthuss mechanism at 85% RH (*E*<sub>a</sub> < 0.4 eV).

Initially, the importance of coordinated H<sub>2</sub>O for proton-conductive MOFs was well studied by Yamada in 2009 using a 1D ferrous oxalate di-hydrate compound.<sup>79</sup> In particular, the coordinated H<sub>2</sub>O in metal (Lewis acid site) increases the acidic with facile proton donation than free H<sub>2</sub>O molecules. As a result, the controlled coordination molecules modulate the proton-conducting property. In 2013, Jeong performed proton conductivity tuning in MOFs through the coordinative insertion methods with protic and aprotic solvent.<sup>82</sup> Following this work, amphoteric organic molecules such as Im<sup>81,128</sup> and urea<sup>80</sup> were used by others for proton conductivity improvement by metal-centre modification. The effect of protic or aprotic molecule coordination for proton conductivity was demonstrated using HKUST-1, [Cu<sub>3</sub>(btc)<sub>2</sub>(H<sub>2</sub>O)<sub>3</sub>], btc<sup>3-</sup> = 1,3,5-benzenetricarboxylate], having Cu-paddlewheel secondary building units (SBUs).<sup>82</sup> The axial sites of the Cu paddle-wheel

ARTICLE

Journal Name

are occupied by H<sub>2</sub>O or EtOH molecules as synthesized. To prepare pure coordination of a solvent, HKUST-1 was activated to generate OMSs, and sequentially pure solvents (H<sub>2</sub>O, EtOH, MeOH, and MeCN) were introduced in the glove box (Fig. 12a). The sample purity was confirmed by <sup>1</sup>H-NMR after the samples were digested in D<sub>2</sub>SO<sub>4</sub>. The conductivity was tested using a pelletized sample under MeOH vapor with N<sub>2</sub> flow at RT. The coordinated EtOH and MeCN have a limited conductivity of 0.2 × 10<sup>-6</sup> S cm<sup>-1</sup>, comparable with dried bulk MeOH (0.17 × 10<sup>-6</sup> S cm<sup>-1</sup>). This implies that neither EtOH nor MeCN is a good candidate for enhancing proton conductivity. However, the coordinated H<sub>2</sub>O has a conductivity of 15 × 10<sup>-6</sup> S cm<sup>-1</sup> that is 75 times larger than the others. This result is attributed to the proton donation from H<sub>2</sub>O and the formation of CH<sub>3</sub>OH<sub>2</sub><sup>+</sup> with autoprotolysis. The lack of a dissociative proton in MeCN and the different acidity of EtOH (pK<sub>a</sub> = 15.9), MeOH (pK<sub>a</sub> = 15.4) from H<sub>2</sub>O (pK<sub>a</sub> = 14) leads to the absence of conductivity enhancement. Instead of MeOH vapor, n-hexane vapor was used as a control experiment. The conductivity of the coordinated H<sub>2</sub>O sample is five orders of magnitude lower than that of MeOH vapor. This study clearly proved the correlation between acidity change and proton conductivity through ligand-accessible metal sites.

In 2017, Ye and Zhang reported an opposite result of proton-conducting property in Im-coordinated Fe-based MOF (Fe-MOF), {Fe<sup>III</sup><sub>2</sub>Fe<sup>II</sup>(μ<sub>3</sub>-O)(CH<sub>3</sub>CO<sub>2</sub>)<sub>6</sub>(H<sub>2</sub>O)<sub>3</sub> as SBUs and [1,1',3',1''-terphenyl]-4,4'',5'-tricarboxylic acid (H<sub>3</sub>L) as ligand},<sup>128</sup> and Cu-based MOF (NENU-3), ([Cu<sub>12</sub>(btc)<sub>8</sub>(H<sub>2</sub>O)<sub>12</sub>][HPW<sub>12</sub>O<sub>40</sub>]-Guest)<sup>81</sup>, respectively, in each individual paper. Cu and Fe-based MOFs show a different SBU like a paddlewheel type for Cu and oxo-bridged three metal clusters for Fe. Both metal clusters can include the OMSs by removal of the coordinated solvents. In a different Im arrangement (guest inclusion or coordinative insertion) in both MOFs, proton conductivity is strongly affected. Fe-MOF was prepared by reaction of a multicarboxylate ligand with a metal cluster [Fe<sub>3</sub>O-(CH<sub>3</sub>CO<sub>2</sub>)<sub>6</sub>], consisting of a small cage with the diameter of 13.2 Å and a bigger cage with the diameter of 22.1 Å. The eight small cages surround the one big cage, resulting in a 3D structure with a 1D circular pore (10 Å) along the c-axis. For the different Im arrangements, the Im involved in the pore as a guest was prepared by simple immersing in Im/ethanol solution (Im@Fe-MOF), including 63 Im molecules/crystal cell. By contrast, the coordinated neutral Im was first prepared from the metal cluster [Fe<sub>3</sub>O-(CH<sub>3</sub>CO<sub>2</sub>)<sub>6</sub>], and then the CH<sub>3</sub>CO<sub>2</sub> in the metal cluster was replaced by a multiple carboxylate ligand for infinite networks (Im-Fe-MOF), including 54 Im molecules/unit cell (Fig. 12b). The coordinated Im protruded to the centre of the cage and reduced the pore size to 5.6 Å. The proton conductivity of Fe-MOF, Im@Fe-MOF, and Im-Fe-MOF was determined by AC impedance spectroscopy at variable temperature and humidity. At 25 °C, 98% RH, Fe-MOF, Im@Fe-MOF, and Im-Fe-MOF show conductivity values of 2.56 × 10<sup>-5</sup>, 8.41 × 10<sup>-5</sup>, and 2.06 × 10<sup>-3</sup> S cm<sup>-1</sup>, respectively. As the temperature increased, conductivity further increased to 1.25 × 10<sup>-4</sup> for Fe-MOF (E<sub>a</sub> = 0.385 eV), 4.23 × 10<sup>-3</sup> (E<sub>a</sub> = 0.573 eV), and 1.21 × 10<sup>-2</sup> S cm<sup>-1</sup> (E<sub>a</sub> = 0.436 eV), respectively, at 60 °C and 98% RH. The pristine sample (Fe-MOF) has low E<sub>a</sub>, implying that the

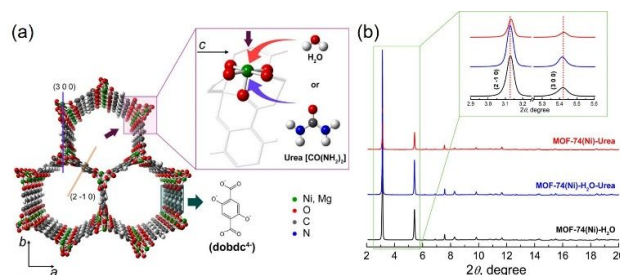


**Fig 13.** (a) Structure of MOF-74(M) and OMS modifications. (b) PXRD patterns. MOF-74(Ni)-H<sub>2</sub>O (black); MOF-74(Ni)-H<sub>2</sub>O-Urea (blue); MOF-74(Ni)-Urea (red). Reproduced from ref.80 with permission from the American Chemical Society, copyright 2020.

absorption of the H<sub>2</sub>O molecule formed an H-bond network among themselves or with coordinated H<sub>2</sub>O. Meanwhile, the occupied Im molecules in the pore of the framework reduced the absorption capacity of H<sub>2</sub>O with interruption of the successive H-bond network, exhibiting high E<sub>a</sub>. Thus, the dominant conduction mechanism of Im@Fe-MOF originated from self-molecular diffusion. To study the conduction mechanism further, a DFT calculation was performed for Fe-MOF and Im-Fe-MOF. The result showed that Im molecules can replace the coordinated H<sub>2</sub>O with an exothermic reaction (-23 kcal mol<sup>-1</sup>) and increase the H<sup>+</sup> concentration by donating H<sup>+</sup> from N-H to the guest H<sub>2</sub>O. The successive H-bond network is attributed to the between the guest H<sub>2</sub>O and coordinated Im because the coordinated adjacent Im has a longer distance than 7.7 Å. In the study of ([Cu<sub>12</sub>(btc)<sub>8</sub>(H<sub>2</sub>O)<sub>12</sub>][HPW<sub>12</sub>O<sub>40</sub>]-Guest)<sup>81</sup>, Im inclusion was performed in two ways: (1) one-step of simple immersion [Im@(NENU-3)] and (2) a two-step process after removal of the coordinated H<sub>2</sub>O and immersion of Im [Im-Cu@(NENU-3a)]. The host framework is isostructural to HKUST-1 encapsulating polyoxometalate anions, exhibiting high hydrothermal and chemical stability. Im@(NENU-3) and [Im-Cu@(NENU-3a)] contain Im molecules at 14.5 wt% and 12.9 wt% in the framework, respectively. The Im-Cu@(NENU-3a) shows a higher proton conductivity (3.16 × 10<sup>-4</sup> S cm<sup>-1</sup> at 70 °C and 90% RH) than pristine NENU-3, but lower than Im-Fe-MOF, which means that bound Im is not a prerequisite for high proton conductivity. However, Im@NENU-3, which includes free Im in the pore, represents the proton conductivity of 1.82 × 10<sup>-2</sup> S cm<sup>-1</sup> at the same conditions, which is higher than that of Im@Fe-MOF. The E<sub>a</sub> of Im@(NENU-3) and Im-Cu@(NENU-3a) were 0.57 eV and 0.79 eV, respectively, indicating vehicle mechanism. The conduction pathway of Im-Cu@(NENU-3) was analysed by single-crystal structure analysis after exposure to H<sub>2</sub>O vapor. According to the structure analysis, the immobilized bound Im isolates the lattice hydrogen, blocking the proton conduction pathway, which results in low conductivity. In contrast, the free Im molecules in the pore can form a continuous H-bond for efficient proton-conducting passage. Nonetheless, the relatively high E<sub>a</sub> of Im@(NENU-3) is thought to be a partial vehicle mechanism from the self-diffusion of protonic free H<sub>3</sub>O<sup>+</sup>. Compared with both studies about Im arrangement in MOF, the channel shape, the pore interconnection, and the distance between adjacent Im

molecules significantly affect proton conductivity in MOFs rather than the coordinative insertion.

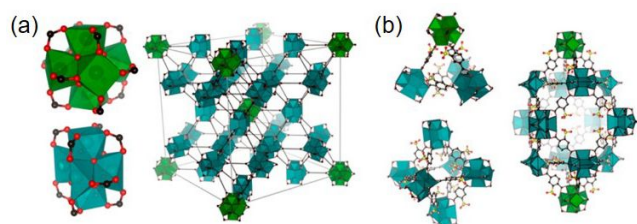


**Fig 14.** (a) Representations of the Zr clusters in  $[Zr_6O_4(OH)_8L_{4.2} \cdot xH_2O]$ , and their connectivity within the unit cell; the 12-connected clusters (green polyhedra) and 9-connected clusters (teal polyhedra) are differentiated. (b) Tetrahedral (top left), octahedral (bottom left), and large pore (right) within  $[Zr_6O_4(OH)_8L_{4.2} \cdot xH_2O]$ . Reproduced from ref.107 with permission from the American Chemical Society, copyright 2015.

In 2020, Marvin and co-workers reported superprotonic conductivity through the solvent-free coordinative urea insertion in MOF-74( $M_2(\text{dobdc}) \cdot H_2O$ ;  $\text{dobdc}^{4-} = 2,5\text{-dioxido-1,4-benzenedicarboxylate}$ ,  $M = \text{Ni}$  and  $\text{Mg}$ )<sup>80</sup> (Fig. 13). The proton conductivity of MOF-74 (Co and Ni) was previously studied by controlling the pH using sulfuric acid ( $H_2SO_4$ ) or aqueous  $NH_3$  treatment, resulting in high proton conductivity ( $10^{-3} \text{ S cm}^{-1}$ ).<sup>129,130</sup> However, the coordinative urea insertion strategy represented superprotonic conductivity ( $10^{-2} \text{ S cm}^{-1}$ ) without any strong acid and base moiety. In general, MOF-74 (M) has a high density of OMS with high structural stability,<sup>131</sup> which is beneficial for coordinative PSMS. The coordinative urea insertion was performed through the solvent-free reaction at the urea melting point to avoid the solvent and moisture coordination in OMS. Depending on the preparation process, four samples were prepared: MOF-74(Ni)- $H_2O$  (fully water coordinated sample), MOF-74(Ni)- $H_2O$ -Urea (partially urea coordinated), MOF-74(Ni)-Urea, and MOF-74(Mg)-Urea (fully urea coordinated sample). With increasing the urea content, the MOFs porosity and aperture size decreased. In contrast to the other samples having a type I  $H_2O$  sorption profile, the fully urea coordinated sample shows a stepwise  $H_2O$  vapor sorption profile with a steep increase around  $P/P_0 = 0.7$  with overall uptake amounts of  $\sim 5 \text{ mol/metal unit}$ . In addition, MOF-74(Mg)-Urea adsorbed higher amounts of  $H_2O$  than MOF-74(Ni)-Urea because of the hydrophilicity. At 298K under 30% RH, the proton conductivity values of four compounds were negligible of  $\sim 10^{-11} \text{ S cm}^{-1}$  for MOF-74(Ni)- $H_2O$  and MOF-74(Ni)- $H_2O$ -Urea and  $\sim 10^{-12} \text{ S cm}^{-1}$  for MOF-74(Ni)-Urea and MOF-74(Mg)-Urea. However, at 298 K and 95% RH, the fully urea coordinated samples indicate a superior increase in proton conductivity values,  $2.64 \times 10^{-2} \text{ S cm}^{-1}$  for MOF-74(Mg)-Urea and  $6.19 \times 10^{-4} \text{ S cm}^{-1}$  MOF-74(Ni)-Urea, although the others are moderate ( $10^{-6} \text{ S cm}^{-1}$ ) under the same conditions. In the trend of humidity dependent  $E_a$ , the  $E_a$  of MOF-74(Mg)-Urea increases up to 1.16 eV at 70% RT, and then starts to decrease up to 0.37 eV at 95% RH, implying a change in the conduction mechanism. By contrast, the  $E_a$  of the other samples (MOF-74(Ni)- $H_2O$  and MOF-74(Ni)- $H_2O$ -Urea) is higher than 0.4 eV in the overall humidity range with vehicular self-diffusion. According to the study of molecular dynamics for  $D_2O@MOF-74(Mg)\text{-Urea-}d_4$

using temperature dependent  $^2H$ -SS NMR, an immobile deuteron signal was observed as a broad anisotropic Pake pattern from bound  $D_2O$  and Urea- $d_4$  at 143 K, indicating a nano ice channel in the pore. As the temperature increases, the majority of  $D_2O$  becomes a mobile state with an isotropic signal, and Urea- $d_4$  represents the small anisotropic signal at RT. This means that the deuteron in Urea- $d_4$  has a slow exchange rate with guest  $D_2O$ , and it is not favoured to be involved in the direct proton transfer process. However, the coordinated urea aids in stabilizing and strengthening the H-bond between guest  $H_2O$  by decreasing the void volume. This system facilitates proton diffusion between guest  $H_2O$  with the Grotthuss mechanism. This study identified the role of urea as excellent assistant for proton diffusion in MOF.

#### Defective metal cluster in MOF

The missing metal centre can provide a local defect and dangling organic linkers, which become proton conduction passages. The defect generation can be classified into intrinsic and extrinsic defects. For the intrinsic defect, the use of an additive during the synthesis of MOFs results in the fine-tuning of properties because of the partial replacement of ligands without change in the overall structure.<sup>132</sup> The extrinsic defects are induced by metal or ligand replacement after MOF synthesis.<sup>133</sup> In 2015, Taylor and coworkers studied the proton-trapping effect in the regular defect in a Zr-based MOF.<sup>107</sup> This Zr MOF was constructed by  $ZrCl_4$  and 2-sulfoterephthalate (L), having a hexanuclear Zr cluster  $[Zr_6O_4(OH)_8L_{4.2} \cdot xH_2O]$ . Based on the Rietveld refinement,  $[Zr_6O_4(OH)_8L_{4.2} \cdot xH_2O]$  has a unit cell parameter of  $a = 41.469$  with an  $Im\bar{3}$  space group, which is approximately double the length of UiO-66 ( $a = 20.7004(2)$ ,  $Fm\bar{3}m$ ) because the vacant site in the metal cluster is located at six of the eight corners of the UiO-66 unit cell. Therefore, two types of metal clusters (9- and 12-connected) are present, and three types of pore exist: a tetrahedral pore ( $\sim 5 \text{ \AA}$ ) with sulfonate occupying the pore window, an octahedral pore ( $\sim 6 \text{ \AA}$ ) with disordered sulfonates occupying the pore space, and a larger pore ( $12 \times 25 \text{ \AA}$ ) from the vacant cluster (Fig. 14). The Zn/S ratio from ICP ( $Zr/S = 1.43$ ) and the determined structure ( $Zr/S = 1.3$ ) have a discrepancy, which means that many atomic positions should be partially occupied, implying the composition of various pore size and cluster type. For an optimal fit, the 9-connected cluster with two ligands and the 12-connected cluster should remain partially occupied and fully occupied, respectively. Thus, the overall formula of 9-connected metal cluster becomes  $Zr_{4.71}O_{5.96}(OH)_{0.44}(R\text{-CO}_2)_{6.48}$ , indicating the reduced occupancy with highly defective structure in the  $T_d$  and  $O_h$  pore. The unusual defect is thought to be the steric hindrance by the bulky sulfonic group and by acidic synthetic conditions. The BET surface area calculated from  $N_2$  sorption is  $1187 \text{ m}^2\text{g}^{-1}$ , and a two-steps  $H_2O$  adsorption isotherm was observed with a total uptake of  $19.7 \text{ mmol g}^{-1}$  at 96.1% RH. The proton conductivities were measured for two batches of samples under the variable temperature (15–65 °C) and humidity. At 65 °C and 95% RH, the conductivities were  $1.93 \times 10^{-3} \text{ S cm}^{-1}$  and  $1.82 \times 10^{-3} \text{ S cm}^{-1}$  with  $E_a$  of 0.25 eV, exhibiting the Grotthuss-type proton diffusion. In contrast, the

conductivity at 30% RH slightly decreased to  $\sim 10^{-4}$  S cm $^{-1}$ . The small reduction in conductivity is thought to be hydrophilic property of the compound. The low conductivity at high humidity and the relatively high conductivity at low humidity are attributed to the trapped proton from sulfonic acid somewhere in the framework. The DFT calculations support that  $\mu_2$ -oxide in the defect is a strong trapping site, revealing a  $pK_a$  of 13.3. The defect-free sites (df-ZrOH or df-SO $_3$ H) do not trap H $^+$  at all. In conclusion, the partial defects decrease the mobile proton concentration, playing the role of an intrinsic buffer. The addition of acid species during MOF synthesis (acetic acid and sulfoacetic acid) or after synthesis (adding guest H $_2$ SO $_4$ ) can reduce the  $pK_a$  of the defect site. Therefore, the inclusion of strong acids (sulfoacetic acid and H $_2$ SO $_4$ ) improves the conductivity to  $5.62 \times 10^{-3}$  ( $E_a = 0.24$  eV) and  $3.46 \times 10^{-3}$  S cm $^{-1}$  at 95% RH, respectively. This study clearly describes the significant effect and role of a defective site in proton conductivity with altering the surface property.

### 3.2 Strategies for manipulating the organic ligand

The various functional group of the ligand can be introduced in MOFs by pre-designed or post-synthetic chemical reactions. In particular, the un-coordinated functional groups have a strong interaction with guest molecules. For proton-conductive MOFs, the introduction of un- or partially coordinated acid functional groups ( $-\text{PO}_3\text{H}_2$ ,  $-\text{SO}_3\text{H}$ , and  $-\text{COOH}$ ) in the ligand became a general approach. Nonetheless, the deliberate production of dangling functional groups is challenging. In addition, the mixed ligand system, the missing connection to the ligand, and PSMs are well-known strategies for proton-conductive MOFs (Fig. 15).

#### Pre-designed ligand functionalization

A representative example of the functional group-dependent proton conductivity was reported by Shigematsu and co-workers in 2011 (Fig. 16).<sup>78</sup> The MIL-53 (Al, Fe) was synthesized by the 1,4-bdc ligand with additional functional groups of  $-\text{NH}_2$ ,  $-\text{OH}$ , and  $-(\text{COOH})_2$  (Fig.16), resulting in MIL-53(Al)-H, MIL-53(Al)-(NH $_2$ ), MIL-53(Al)-(OH), and MIL-53(Fe)-(COOH) $_2$ . The well-known structure of MIL-53 (M) has a 1D metal chain bridged by  $-\text{OH}$ , and a bdc ligand connects the metal centre to construct a 3D network. The additional functional groups protrude into the pore direction, and the difference in functional groups (R) affects the acidity ( $pK_a$ ) of frameworks (the  $pK_a$  values of meta-substituted R functional group given by the Hammett relation<sup>134</sup> are 4.74 for  $-\text{NH}_2$ , 4.19 for  $-\text{H}$ , 4.08 for  $-\text{OH}$ , and 3.62 for  $-\text{COOH}$ , respectively). In H $_2$ O

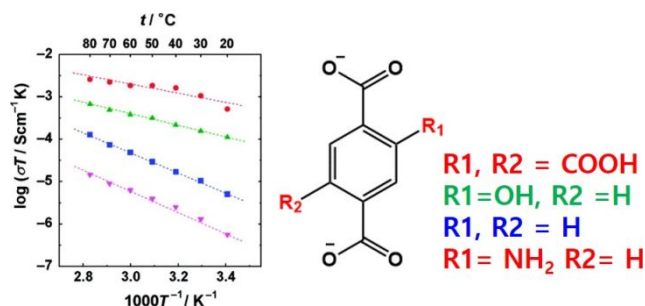


**Fig 16.** Arrhenius plots of the proton conductivities of MIL-53(Al) (blue), MIL-53(Al)-(NH $_2$ ) (pink), MIL-53(Al)-(OH) (green), and MIL-53(Fe)-(COOH) $_2$  (red) under 95% RH. Least-squares fits are shown as dotted lines. The bdc ligand with different functional groups is reproduced from ref.78 with permission from the American Chemical Society, copyright 2011.

vapor sorption, MIL-53(Al)-(OH), shows a “breathing effect,” which means that pore size changes from a narrow pore (NP) to a large pore (LP), with the highest uptake amounts (5 mol per metal unit) among the samples. The others uptake 1 H $_2$ O molecules for MIL-53(Al)-H, 1 for MIL-53(Al)-(NH $_2$ ), and 1.5 mol per metal unit for MIL-53(Fe)-(COOH) $_2$ . In contrast to the H $_2$ O absorption capacity, the proton conductivities at 298 K and 95% RH were in the order of MIL-53(Fe)-(COOH) $_2$ , MIL-53(Al)-(OH), MIL-53(Al)-H, and MIL-53(Al)-(NH $_2$ ) with the values of  $2.0 \times 10^{-6}$  for MIL-53(Fe)-(COOH) $_2$ ,  $4.2 \times 10^{-7}$  S cm $^{-1}$  for MIL-53(Al)-(OH),  $2.3 \times 10^{-8}$  for MIL-53(Al)-H and  $2.3 \times 10^{-9}$  S cm $^{-1}$  for MIL-53(Al)-(NH $_2$ ), respectively. This means that conductivity is significantly correlated to the acidity of the framework and the excess H $_2$ O represents a minor contribution to improve the conductivity. A plausible conduction pathway is considered to be the H-bond network in the guest H $_2$ O,  $\mu_2$ -OH, and the  $-\text{COOH}$  functional group. In 2014, Yamada studied the control of proton conductivity and H $_2$ O adsorption capacity in a single phase of Al(OH)(bdc-OH) $_x$ (bdc-NH $_2$ ) $_{1-x}$  (MIL-53 derivative) constructed by the mixed ligand of 1,4-bdc-NH $_2$  and 1,4-bdc-OH with a different ratio.<sup>135</sup> All compounds with different ligand ratios indicate an NP state under ambient humidity. If the portion of x is larger than 0.5, an LP transition occurs in the MOFs during the H $_2$ O adsorption, which is reflected in a different gate-opening pressure in the H $_2$ O. It is derived from the different H $_2$ O adsorption capacity in pure compounds of each ligand. The increased bdc-OH portion decreases gate opening pressure. The conductivity values of Al(bdc-OH) $_x$ (bdc-NH $_2$ ) $_{1-x}$  depend on the adsorbed amounts of water, implying the dominant contribution of guest H $_2$ O in the formation of the H-bond. The maximum proton conductivity of Al(bdc-OH) $_x$ (bdc-NH $_2$ ) $_{1-x}$  cannot exceed that of pure Al(OH)(bdc-OH) ( $\sim 10^{-6}$  S cm $^{-1}$ ), which has the highest H $_2$ O adsorption capacity. Nonetheless, the controlled ligand ratio induces the H $_2$ O adsorption amounts, resulting in the fine-tuning of the proton conductivity in the range of  $10^{-9} \sim 10^{-6}$  S cm $^{-1}$ .

#### Defect of the ligand in MOF

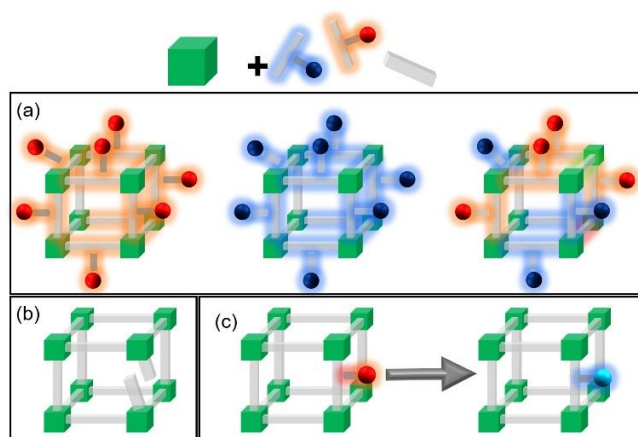


**Fig 15.** Schematic illustration of the strategies for manipulating organic ligands. (a) pre-designed functionalization and mixed ligand system; (b) ligand missing or missing connection; (c) post-synthetic functional group modification.

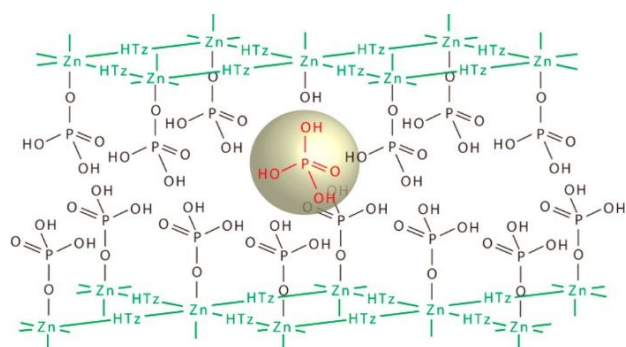


**Fig 17.** Proposed structural model of **5**.  $\text{OH}^-$  is coordinated to Zn instead of monodentate  $\text{H}_2\text{PO}_4^-$ , whereas the uncoordinated  $\text{H}_3\text{PO}_4$  occupies the space where the monodentate  $\text{H}_2\text{PO}_4^-$  existed. Reproduced from ref.108 with permission from the American Chemical Society, copyright 2016.

In 2016, Inukai and co-workers demonstrated the enhanced anhydrous proton conductivity in defective ligand sites where the proton carriers are encapsulated.<sup>108</sup> Initially, they synthesized a non-porous 2D coordination polymer,  $[\text{Zn}(\text{H}_2\text{PO}_4)_2(\text{TzH})_2]_n$ , where, TzH connects the metal centre and mono-dentate  $\text{H}_2\text{PO}_4^-$  ions are the dominant proton pathway for proton hopping (Fig. 17). As a general strategy for increasing the proton concentration and mobility, the defect was introduced in a mono-dentate  $\text{H}_2\text{PO}_4^-$  site, and mobile  $\text{H}_3\text{PO}_4$  species were encapsulated. The amounts of  $\text{H}_3\text{PO}_4$  reacted were 4.0 for **2**, 4.4 for **3**, 4.8 for **4**, and 5.2 mmol for **5**, leading to the difference of the elemental ratio in the framework due to the defect formation (defect-free compound has an elemental ratio of Zn (1): P(1): C (4): N (6)). The defective frameworks have a lower P content with similar C and N ratios, and compound **5** has a P ratio that is similar to the defect-free sample, implying the presence of uncoordinated  $\text{H}_2\text{PO}_4^-$  in the defect of a mono-dentate  $\text{H}_2\text{PO}_4^-$  site. This type of defect was difficult to distinguish using PXRD due to a similar pattern without additional peaks except compound **2**. Compound **2** shows an additional peak at  $10.5^\circ$ , suggesting a partial change in the structure around the defect. The compounds are stable at  $150^\circ\text{C}$  without a structural transformation. The embedded  $\text{H}_3\text{PO}_4$  is retained in the framework until the decomposition temperature ( $180^\circ\text{C}$ ). The conductivity of defective compounds (**2–5**) was measured at variable temperature ( $30\text{–}150^\circ\text{C}$ ) under a  $\text{N}_2$  atmosphere. As the temperature increased, the proton conductivity was increased with increasing ratio of reacted  $\text{H}_3\text{PO}_4$ , and the  $\text{H}_3\text{PO}_4$  encapsulation decreased the  $E_a$  values (0.85, 0.57, 0.52, and 0.53 eV for **2**, **3**, **4**, and **5**, respectively). Compound **5**, where  $\text{H}_3\text{PO}_4$  was embedded in the defect, shows the highest conductivity of  $4.6 \times 10^{-3} \text{ S cm}^{-1}$  at  $150^\circ\text{C}$ , which is four orders of magnitude higher than that of compound **2** and one order higher than that of defect-free compound ( $1.2 \times 10^{-4} \text{ S cm}^{-1}$  at  $150^\circ\text{C}$ ). In  $\text{H}_2/\text{O}_2$  FC test, the maximum OCV for compound **5** is 0.88 V for 1 h, slightly lower than the theoretical maximum of 1.16 V. It implies the fuel crossover phenomenon and side chemical reaction. The mobile proton carriers are clearly observed by  $^{31}\text{P}$  solid state-magic angle spinning (MAS) NMR with and without cross-polarization between  $^1\text{H}$  and  $^{31}\text{P}$ . In contrast to the defect-free single-crystal structure, all defective samples indicate two phosphorous peaks at  $-3.2$  and

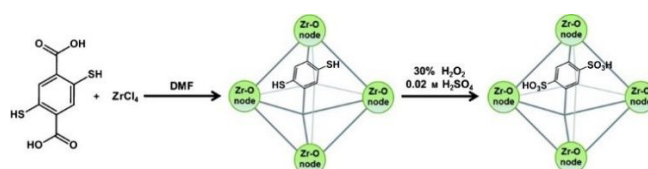


**Fig 18.** Synthesis of UiO-66(SH)<sub>2</sub> and post-synthetic oxidative modification of UiO-66(SH)<sub>2</sub> to UiO-66(SO<sub>3</sub>H)<sub>2</sub>. DMF = *N,N*-dimethylformamide. Reproduced from ref.83 with permission from Wiley-VCH, copyright 2015.

$-5.7$  ppm, which is attributed to the P of  $\text{H}_2\text{PO}_4^-$  near the coordinated  $\text{OH}^-$ . It clearly proves the presence of a defect in the frameworks. In addition, compounds **4** and **5** show additional peaks at 0.00 and  $-11.4$  ppm, implying the presence of uncoordinated  $\text{H}_3\text{PO}_4$  and  $\text{H}_2\text{PO}_4^-$ . These mobile species provide a new proton-hopping path with low  $E_a$ . This work provides a systematic study and various characterization tools for detecting defect sites and mobile species for proton-conductive MOFs.

#### Post-synthetic ligand functionalization

In general, the multiple O atoms in the ligand act as metal coordination sites during the MOF synthesis. Therefore, the acidic functional groups ( $-\text{COOH}$ ,  $-\text{SO}_3\text{H}$ , and  $-\text{PO}_4\text{H}_3$ ) are fully or partially coordinated to the metal centre with a restricted role as proton donors. To avoid this limitation, the post-synthetic chemical reaction after the MOF synthesis is a useful

approach. In 2015, Phang and co-workers induced the acidic site in UiO-66-(SH)<sub>2</sub> by converting -SH into -SO<sub>3</sub>H through a post-synthetic oxidation reaction.<sup>83</sup> The UiO-66-type MOF has moisture and chemical stability because of the multiple ligand coordination with the large metal cluster formation. The initial compound, UiO-66-(SH)<sub>2</sub>, is identical structure to UiO-66. To convert the -SH functional group to -SO<sub>3</sub>H, the oxidation reaction was performed with H<sub>2</sub>O<sub>2</sub> for 1 h, and sequential protonation was carried out using 0.02 M H<sub>2</sub>SO<sub>4</sub> solution. During the chemical reaction, there was no change or decomposition in the frameworks. The additional functional groups were confirmed by X-ray photoelectron spectra (XPS) and IR spectra, resulting in the higher binding energy of S, 2P<sub>3/2</sub> (167.8 eV). The change in bulkiness of -SO<sub>3</sub>H is reflected in the reduced surface area from 308 m<sup>2</sup>g<sup>-1</sup> to 35 m<sup>2</sup>g<sup>-1</sup> by N<sub>2</sub> sorption at 77 K. Moreover, UiO-66-(SO<sub>3</sub>H)<sub>2</sub> indicates steep H<sub>2</sub>O adsorption with a large hysteresis, suggesting strong interaction between the framework and guest H<sub>2</sub>O molecules. The proton conductivity was measured at variable temperature (25–80 °C) under 90% RH. As expected, the pristine compound (UiO-66-(SH)<sub>2</sub>) indicated the relatively low conductivity of ~10<sup>-6</sup> S cm<sup>-1</sup> at 25 °C at 90% RH, while UiO-66(SO<sub>3</sub>H)<sub>2</sub> exhibited 1.4 × 10<sup>-2</sup> S cm<sup>-1</sup> at the same condition and the conductivity improved to 8.4 × 10<sup>-2</sup> S cm<sup>-1</sup> at 80 °C with low E<sub>a</sub> of 0.32 eV, corresponding to the Grotthuss mechanism. A steep increase in proton conductivity was observed above 50% RH in humidity-dependent conductivity measurement, indicating the H<sub>2</sub>O-mediated proton conduction passage. In the post-synthetic modification, the structural stability is a prerequisite to avoid decomposition during the chemical reaction. This work achieved efficient and stable conductivity by judicious selection of stable host materials and chemical reaction for post-chemical modification.

### 3.3 Strategies for manipulating the pore space

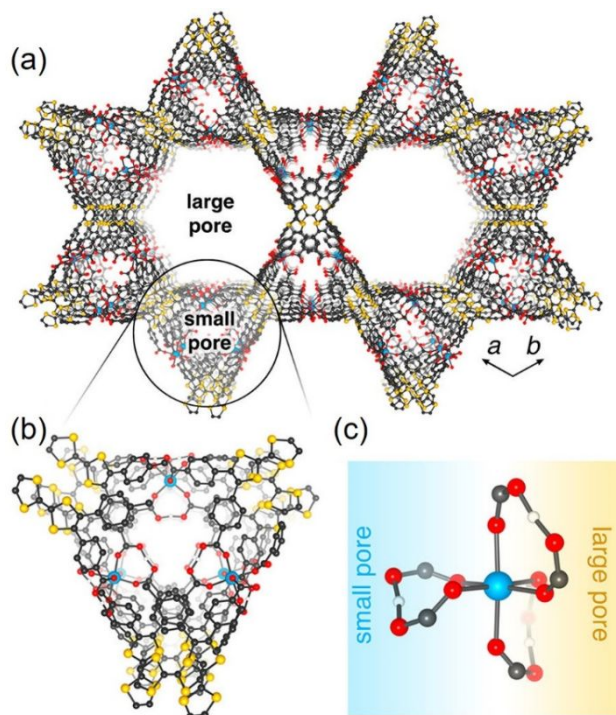


**Fig 19.** (a) Crystal structure of Mg<sub>2</sub>H<sub>6</sub>(H<sub>3</sub>O)(TTFTB)<sub>3</sub> (MIT-25) viewed along the c-axis. (b) The small pore contains protruding H-bonded protons. (c) The local coordination environment of each Mg<sup>2+</sup> centre: one μ<sub>2</sub>-H-bridged carboxylic acid points into the small pore and two μ<sub>2</sub>-H-bridged carboxylic acids run along the walls of the large pore. Reproduced from ref.138 with permission from the American Chemical Society, copyright 2015.

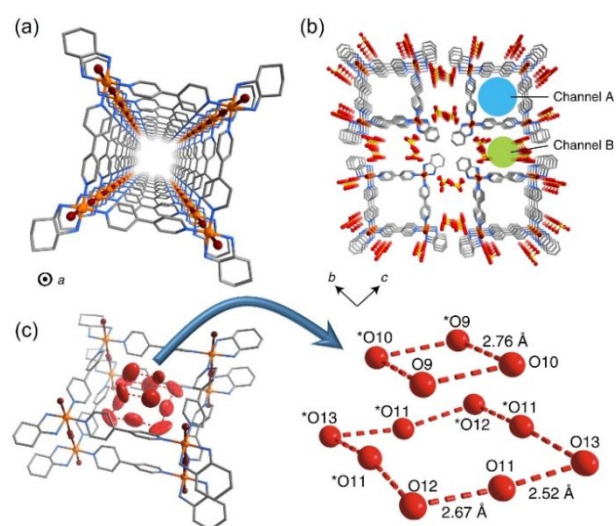


**Fig 20.** (a) The four-legged tubular structure of [Pt(dach)(bpy)Br]<sub>4</sub>(SO<sub>4</sub>)<sub>4</sub>·32H<sub>2</sub>O viewed along the a-axis (100 K). Counter anions and water molecules have been omitted for clarity. (b) The packing structure of 1 in the bc plane. Channels A and B are highlighted by light blue and light green circles, respectively. (c) Tetramer and octamer-like water clusters in tubular structure. Reproduced from ref.146 with permission from Nature Research, copyright 2020.

Compared with other materials, one of the critical characteristics in crystalline MOFs is high porosity. Thus, the simplest manipulation of the pore to fabricate the proton-conductive MOFs is thought to be the incorporation of conducting media in a void space. According to previous studies, the representative proton-conductive MOFs are related to the inclusion of amphoteric guests or acidic guest molecules such as Im, triazole, H<sub>2</sub>SO<sub>4</sub>, H<sub>3</sub>PO<sub>4</sub>, toluenesulfonic acid, trifluoromethanesulfonic acid, and imidazolium/benzimidazolium triflates.<sup>18,24,84,136,137</sup> Therefore, guest inclusion is considered a common pore manipulation strategy. However, in this section, we focus on pore design and environment rather than the simple encapsulation of guest molecules as manipulation of pore space. The pore design and environment intimately depend on the selection of ligands and their functional groups. As a result, the hydrophilic or hydrophobic surface affects the flexible H-bonding interaction between the conducting media and surface of frameworks, improving the proton conductivity and conduction mechanism.

#### Proton conduction in hydrophilic pore

In 2018, Park and co-workers reported on the selective vapor pressure-dependent proton transport in mesoporous MOF.<sup>138</sup> Mesoporous MOF (MIL-25, Mg<sub>2</sub>H<sub>6</sub>(H<sub>3</sub>O)(TTFTB)<sub>3</sub>) with two distinct channels was synthesized by Mg<sup>2+</sup> and the tetrathiafulvalene-tetrabenzoate (TTFTB<sup>4-</sup>) ligand (Fig. 19). This compound has two cylindrical pores with 27 and 4.5 Å diameter for the large and small pore, respectively. The hexagonal shape of a large pore is surrounded by μ<sub>2</sub>-H-bridged carboxylic acids coordinated to Mg<sup>2+</sup>, and the small pore includes the additional μ<sub>2</sub>-H-bridged carboxylate toward pore direction with the stoichiometric H<sub>3</sub>O<sup>+</sup> ion, forming a helical channel. In H<sub>2</sub>O vapor sorption, there is characteristic stepwise adsorption. The first

step occurred below 40% RH in hydrophilic pore (small pore), whereas the second step above 50% RH was related to a less hydrophilic pore with a large void space. At high pressure, structural swelling is observed without saturation, implying further oxidation of the TTF ligand. The computational DFT calculation of electrostatic potential and pore volume provides insight into H<sub>2</sub>O filling a small pore at low pressure. The calculated electrostatic volume for a small pore is  $\sim 156 \text{ \AA}^3$ , which is the subtracted volume of the occupied 1.5 H<sub>3</sub>O<sup>+</sup> ions, and approximately 7.5 H<sub>2</sub>O guest molecules can be accommodated in the void space. This result is coincident with experimental observations (5 mmol<sub>H<sub>2</sub>O</sub>/mol<sub>MOF</sub> at low RH). The

potential proton conductivity was investigated in a pelletized sample under variable temperature and humidity. At 40% RH and 25 °C, the proton conductivity was  $1.58 \times 10^{-5} \text{ S cm}^{-1}$ , and increased to  $1.03 \times 10^{-4} \text{ S cm}^{-1}$  at 75 °C with an  $E_a$  of 0.36 eV. In addition, the conductivity at 95% RH and 25 °C is  $6.8 \times 10^{-5} \text{ S cm}^{-1}$  and  $5.1 \times 10^{-4} \text{ S cm}^{-1}$  at 75 °C with  $E_a$  of 0.40 eV. Despite the negligible difference in  $E_a$ , the trend of increasing  $E_a$  suggested a change in the conduction mechanism or pathway.

ARTICLE

**Table 1.** Comparison of performance in proton conductive MOFs

Compound	Structural dimensionality	Condition	Conductivity/ S cm <sup>-1</sup> ( $E_a$ , eV)	Type of design	ref
HKUST-1 [Cu <sub>3</sub> (btc) <sub>2</sub> (H <sub>2</sub> O) <sub>3</sub> ]-H <sub>2</sub> O	3D	RT/ MeOH Flow	<sup>a</sup> 1.5 × 10 <sup>-6</sup>	Metal centre manipulation	82
Urea-MOF-74 (Mg)	3D	95% RH 55 °C	<sup>a</sup> 3.69 × 10 <sup>-2</sup> (0.14)	Metal centre manipulation	80
Urea-MOF-74 (Ni)	3D	95% RH 55 °C	<sup>a</sup> 2.34 × 10 <sup>-3</sup> (0.37)	Metal centre manipulation	80
Cr-MIL-88B-PESE	3D	85% RH 100 °C	<sup>a</sup> 4.50 × 10 <sup>-2</sup> (0.34)	Metal centre manipulation	126
Cr-MIL-88B-PSA	3D	85% RH 100 °C	<sup>a</sup> 1.58 × 10 <sup>-1</sup> (0.38)	Metal centre manipulation	126
Im-Fe-MOF	3D	98% RH 60 °C	<sup>a</sup> 4.50 × 10 <sup>-2</sup> (0.44)	Metal centre manipulation	128
IM-{Fe <sup>III</sup> <sub>2</sub> Fe <sup>II</sup> (μ <sub>3</sub> -O)(CH <sub>3</sub> CO <sub>2</sub> ) <sub>6</sub> (H <sub>2</sub> O) <sub>3</sub> }					
Im-NENU	3D	98% RH 70 °C	<sup>a</sup> 3.16 × 10 <sup>-4</sup> (0.79)	Metal centre manipulation	81
Im-([Cu <sub>12</sub> (btc) <sub>8</sub> (H <sub>2</sub> O) <sub>12</sub> ][HPW <sub>12</sub> O <sub>40</sub> ])					
Ferrous oxalate dihydrate Fe(ox)·2H <sub>2</sub> O	1D	98% RH 25 °C	<sup>a</sup> 1.3 × 10 <sup>-3</sup> (0.37)	Metal centre manipulation	79
Mg-OBA, [Mg <sub>2</sub> (OBA) <sub>2</sub> (H <sub>2</sub> O) <sub>6</sub> ·2H <sub>2</sub> O] <sub>n</sub>	2D	95% RH 80 °C	<sup>a</sup> 1.27 × 10 <sup>-2</sup> (0.13)	Metal centre manipulation	139
[Zn <sub>3</sub> (H <sub>2</sub> PO <sub>4</sub> ) <sub>6</sub> ·(Hbim)]	1D	Anhydrous, 120 °C	<sup>a</sup> 1.3 × 10 <sup>-3</sup>	Ligand functionalization	140
Defective [Zn(H <sub>2</sub> PO <sub>4</sub> ) HTz <sub>2</sub> ] <sub>n</sub>	2D	Anhydrous, 150 °C	<sup>a</sup> 3.16 × 10 <sup>-3</sup>	Ligand defect	108
MIL-53(Al)-NH <sub>2</sub> , [Al(OH)(BDC-NH <sub>2</sub> )]	3D	95% RH, 80 °C	<sup>a</sup> 4.1 × 10 <sup>-8</sup> (0.45)	Ligand functionalization	78
MIL-53(Al)-OH, [Al(OH)(BDC-OH)]	3D	95% RH, 80 °C	<sup>a</sup> 1.9 × 10 <sup>-6</sup> (0.27)	Ligand functionalization	78
MIL-53(Fe)-COOH <sub>2</sub> , [Fe(OH)(BDC-(COOH) <sub>2</sub> )]	3D	95% RH, 80 °C	<sup>a</sup> 7 × 10 <sup>-6</sup> (0.21)	Ligand functionalization	78
UiO-66(SO <sub>3</sub> H) <sub>2</sub> , Zr <sub>6</sub> O <sub>4</sub> (OH) <sub>4</sub> (BDC-(SO <sub>3</sub> H) <sub>2</sub> ) <sub>6</sub>	3D	90% RH, 80 °C	<sup>a</sup> 8.4 × 10 <sup>-2</sup> (0.32)	Ligand functionalization	83
PCMOF10, Mg <sub>2</sub> (H <sub>2</sub> O) <sub>4</sub> (H <sub>2</sub> L)·H <sub>2</sub> O	2D	95% RH, 70 °C	<sup>a</sup> 3.55 × 10 <sup>-2</sup> (0.4)	Ligand functionalization	141
L = 2,5-dicarboxy-1,4-benzenediphosphonic acid					
BUT-8-(Cr)A,	3D	80 °C, 100% RH	<sup>a</sup> 1.27 × 10 <sup>-1</sup> (0.11)	Ligand functionalization	76
Cr <sub>3</sub> (μ <sub>3</sub> -O)(H <sub>2</sub> O) <sub>3</sub> (NDC(SO <sub>3</sub> H <sub>5/6</sub> ) <sub>2</sub> ) <sub>3</sub>					
PCMOF-20. (DMA) <sub>3</sub> [Zr(HL)F <sub>2</sub> ] H <sub>6</sub> L = 2,4,6-tris(4-phosphonophenyl) pyridine	2D	80 °C, 95% RH	<sup>a</sup> 1.0 × 10 <sup>-2</sup> (0.2)	Ligand functionalization	142
Co-fdc, {[Co(bpy)-(H <sub>2</sub> O) <sub>4</sub> ](fdc)-(H <sub>2</sub> O) <sub>1.5</sub> ] <sub>n</sub>	1D	80 °C, 98% RH	<sup>a</sup> 4.85 × 10 <sup>-3</sup> (0.4)	Ligand functionalization	143
Co-tri {[Co(bpy)-(H <sub>2</sub> O) <sub>4</sub> ](Hbtc)(H <sub>2</sub> O) <sub>1.5</sub> ] <sub>n</sub>	1D	80 °C, 98% RH	<sup>a</sup> 1.49 × 10 <sup>-1</sup> (0.4)	Ligand functionalization	143
Co-tetra {[Co(bpy)(H <sub>2</sub> O) <sub>4</sub> ](btcc) <sub>0.5</sub> ·H <sub>2</sub> O] <sub>n</sub>	1D	80 °C, 98% RH	<sup>a</sup> 4.15 × 10 <sup>-2</sup> (0.29)	Ligand functionalization	143
BUT-83, [Co(DCDPP)]·5H <sub>2</sub> O	3D	80 °C, 97% RH	<sup>a</sup> 3.9 × 10 <sup>-2</sup> (0.34)	Ligand functionalization	144
Mg <sub>2</sub> H <sub>6</sub> (H <sub>3</sub> O)(TTFTB) <sub>3</sub>	3D	95% RH 75 °C	<sup>a</sup> 5.1 × 10 <sup>-4</sup> (0.4)	Hydrophilic Pore	138
NMe <sub>3</sub> (CH <sub>2</sub> COOH)[FeCr(ox) <sub>3</sub> ]	2D	65% RH 25 °C	<sup>a</sup> 8 × 10 <sup>-4</sup>	Hydrophilic Pore	77
dic-MnCr, {NBu <sub>2</sub> (CH <sub>2</sub> COOH) <sub>2</sub> }[MnCr(ox) <sub>3</sub> ]	2D	98% RH 25 °C	<sup>a</sup> 1.8 × 10 <sup>-3</sup> (0.31)	Hydrophilic layer	145
[Pt(dach)(bpy)Br] <sub>4</sub> (SO <sub>4</sub> ) <sub>4</sub> ·32H <sub>2</sub> O	pseudo1D	95% RH 55 °C	<sup>b</sup> 1.7 × 10 <sup>-2</sup> (0.22)	Hydrophobic Pore	146
Im@Fe-MOF	3D	98% RH 60 °C	<sup>a</sup> 4.23 × 10 <sup>-3</sup> (0.57)	Guest inclusion	128
IM-{Fe <sup>III</sup> <sub>2</sub> Fe <sup>II</sup> (μ <sub>3</sub> -O)(CH <sub>3</sub> CO <sub>2</sub> ) <sub>6</sub> (H <sub>2</sub> O) <sub>3</sub> }					
Im@NENU	3D	98% RH 70 °C	<sup>a</sup> 1.82 × 10 <sup>-2</sup> (0.57)	Guest inclusion	81
Im@([Cu <sub>12</sub> (btc) <sub>8</sub> (H <sub>2</sub> O) <sub>12</sub> ][HPW <sub>12</sub> O <sub>40</sub> ])					
Ca-PiPhtA-NH <sub>3</sub>	3D	98% RH, 24 °C	<sup>a</sup> 6.6 × 10 <sup>-3</sup> (0.40)	Guest/Ligand functionalization	147
MOF-74(Co)	3D	pH11, 90 °C, c-axis	<sup>b</sup> 4.5 × 10 <sup>-3</sup> (0.12)	Guest inclusion	130
H <sup>+</sup> @Ni <sub>2</sub> (dobdc), Ni <sub>2</sub> (dobdc)(H <sub>2</sub> O) <sub>2</sub>	3D	95% RH, 80 °C	<sup>a</sup> 2.2 × 10 <sup>-2</sup> (0.25)	Guest inclusion	129
H <sub>3</sub> PO <sub>4</sub> @MIL-101, H <sub>3</sub> PO <sub>4</sub> @Cr <sub>3</sub> O(H <sub>2</sub> O) <sub>3</sub> (BDC)	3D	150 °C	<sup>a</sup> 3.0 × 10 <sup>-3</sup> (0.25)	Guest inclusion	84
Im@MOF-217, [Ti(TDHT)	3D	Anhydrous, 100 °C	<sup>a</sup> 1.1 × 10 <sup>-3</sup> (0.58)	Guest inclusion	148
(Me <sub>2</sub> NH <sub>2</sub> ) <sub>1.58</sub> (DMF) <sub>0.15</sub> (MeOH) <sub>0.5</sub> (NBu <sub>4</sub> Br) <sub>0.15</sub> (H <sub>2</sub> O) <sub>2.25</sub>					
H <sub>2</sub> SO <sub>4</sub> @MIL-101-SO <sub>3</sub> H	3D	90% RH, 70 °C	<sup>a</sup> 1.82 (0.21)	Guest/Ligand functionalization	18
(Me <sub>2</sub> NH <sub>2</sub> )[Eu(L)] (H <sub>4</sub> L = 5-(phosphonomethyl)isophthalic acid)	2D	98% RH, 100 °C	<sup>a</sup> 3.76 × 10 <sup>-3</sup> (0.72)	Counter ions	92

*a* = pelletized sample, *b* = single crystal.

## ARTICLE

According to the H<sub>2</sub>O vapor sorption and computational study, the small pore can be occupied by guest H<sub>2</sub>O at 40% RH, which means that the conductivity at low humidity is mainly attributed to the Grotthuss mechanism in the hydrophilic small pore. However, the conductivity at high RH involves an average of the large and small pores due to the sequential filling of large and small pore. Although it is difficult to understand the conduction mechanism in large pore only using  $E_a$ , the increase of  $E_a$  value as humidity increase provides an intuition of the increased contribution of vehicular diffusion in the conduction mechanism. This study provides observation of structure (pore surface and size)–function relationship in proton conductive MOF. In addition, it emphasized the importance of the hydrophilic pore design.

#### Proton conduction in hydrophobic pore

In 2020, Otake and co-workers reported the design of a hydrophobic channel, a confined H<sub>2</sub>O cluster, and its proton conductivity in metal-organic nanotube (Fig. 20).<sup>146</sup> Due to the limited number of H-bond, H<sub>2</sub>O the confined in hydrophobic nanochannel (< 3–4 nm) can show the unusual structure and MD never seen in the bulk state (liquid phase).<sup>149</sup> The carbon nanotube was a representative system for a hydrophobic nanochannel. However, direct observation of the H<sub>2</sub>O cluster and proton transport in the channel is challenging because of pore crystallinity. The metal-organic nanotube, [Pt(dach)(bpy)Br]<sub>4</sub>(SO<sub>4</sub>)<sub>4</sub> · 32H<sub>2</sub>O (dach: (1R,2R)-(–)-1,2-diaminocyclohexane; bpy: 4,4'-bipyridine), was synthesized by oxidative polymerization of square planar Pt complexes with Br<sub>2</sub>. The Pt metal was connected by a bpy ligand, resulting in a rectangular shape of [Pt(dach)(bpy)]<sub>4</sub> with +8 net charge, where the axial sites of Pt were bridged by the halogen (Br) atom, forming the overall MX tube. The channel was occupied by H<sub>2</sub>O molecules clustering in a tetramer and octamer with alternating arrangement, as verified by single-crystal X-ray analysis. For the charge balance, four counter sulfate anions are located between channels. Therefore, there are two types of channels, a hydrophobic inner tube (channel A) and a hydrophilic between-tube (channel B) (Fig. 20b). In channel A, H<sub>2</sub>O molecules hold each other with an O–O distance of 2.5–2.7 Å and a weak H-bond between the clusters with a distance of 3.0–3.4 Å. In particular, the H<sub>2</sub>O molecules inside the channel are at a distance of > 2.9 Å away from the wall, implying weak interaction. To understand the potential proton conductivity through the H<sub>2</sub>O channel, AC impedance was measured using a single crystal under variable humidity (40–95 % RH) and temperature. At 55 °C and 95 % RH, the proton conductivity along the channel direction was  $1.7 \times 10^{-2} \text{ S cm}^{-1}$  with an  $E_a$  of 0.22 eV, two orders of magnitude higher than the pelletized

sample under the same conditions, which means an anisotropic proton conduction in the presence of a conduction pathway in the channel direction. Nonetheless, the grain boundary effect of pelletized sample cannot be ignored. A plausible conduction mechanism was identified by <sup>1</sup>H-SS-NMR measurement. <sup>1</sup>H-MAS NMR spectra indicate a single component of crystallized H<sub>2</sub>O and an <sup>1</sup>H-pulsed-field gradient (PFG) NMR provided the proton diffusion coefficients of  $2.9 \times 10^{-11} \text{ m}^2\text{s}^{-1}$  (in the channel direction) and  $1.6 \times 10^{-12} \text{ m}^2\text{s}^{-1}$  (perpendicular to the channel). The proton diffusivity calculated by quantum-mechanical molecular dynamics (QM-MD) simulations indicated that the vehicular diffusion coefficients ( $D_v$ ) and the Grotthuss diffusion coefficient ( $D_G$ ) in channel A are 1.5 and 2 times faster than that of channel B, respectively. The overall proton diffusion-coefficient ( $D_p$ ) in the hydrophobic channel is in the middle of the liquid and solid-state. This study showed a high proton conductivity in the hydrophobic channel design without introducing a strong acidic moiety. In addition, various characterization tools and computational studies support the importance of the pore environment for proton diffusion.

## 4. Conclusion and perspectives

The porous metal-organic frameworks have become a platform for various applications. In particular, the proton-conductive MOFs are steeply growing during the last decade and are increasing year-by-year with advanced achievements (Fig. 21). This review discussed the various strategies from the design of frameworks to pore environment and unique studies for proton-conductive MOFs with representative examples.

From previous reports, we concluded the required features for proton-conductive MOFs with high conductivity to be follows: (1) Robustness of framework; the backbone of the framework should be retained during any manipulation at least in the hydration and dehydration processes. (2) The ordered protic site for proton-donating and regular hydrogen bonding. (3) Impregnation of high carrier density. The acidic struts with acid functional groups such as carboxylate, phosphonate, and sulfonate are promising components for the design of proton-conductive MOFs.<sup>150–152</sup> Moreover, the encapsulation of acid guests in void space becomes a more general approach in this field. To date, some of the works present high conductivities (>  $10^{-1} \text{ S cm}^{-1}$ ), which are comparable to the conventional material. Nonetheless, there are still barriers to practical use, such as structural stability, fabrication of membrane, grain boundary effect, and the fuel crossover effect. In addition, the limited operating temperature is a challenge.

From the perspective of research in proton-conductive MOFs, (1) mining of potential candidates from the big data system of the structure reported is important as a future endeavour. (2) The design of potential conducting pathways through a flexible structure, which is superficially invisible and can respond to external stimuli, is helpful for a strong H-bond network under the low humidity condition. (3) From a structural point of view, a small aperture and large cavity might be useful to prevent the escaping the conducting media and to encapsulate a large amount of conducting media in the cavity. Indeed, it will be beneficial for reducing the fuel crossover. (4) The design of directional proton diffusion through the  $pK_a$  gradient might provide opportunities to create new materials. (5) The high proton conductivity at sub-zero temperature and

BUT = Beijing University of Technology  
 NNU = Nanjing Normal University  
 MIL = Material from Institut Lavoisier  
 HKUST = Hong Kong University of Science and Technology  
 OCV = open circuit voltage  
 DFT = density functional theory  
 MD = molecular dynamics  
 MOP = metal organic polyhedral  
 MOF = metal organic framework  
 RMOFs = rigid structural MOFs  
 NP = narrow pore  
 LP = large pore  
 adp = adipic acid  
 bpy = 4,4'-bipyridine  
 btc<sup>3-</sup> = 1,3,5-benzenetricarboxylate  
 dach = (1R,2R)-(-)-1,2-diaminocyclohexane  
 dobdac<sup>4-</sup> = 2,5-dioxido-1,4-benzenedicarboxylate  
 fdc = furan di-carboxylate  
 Hbim = benzimidazole  
 H<sub>2</sub>DCDPP = 5,15-di(4-carboxylphenyl)-10,20-di(4-pyridyl)porphyrin  
 NDC(SO<sub>3</sub>H)<sub>2</sub> = 4,8- disulfonaphthalene-2,6-dicarboxylate  
 1,4-bdc = 1,4-benzenedicarboxylate  
 OBA = 4,4'-oxybis(benzoic acid)  
 ox<sup>2-</sup> = oxalate  
 PiPhtA = 5-(dihydroxyphosphoryl)isophthalic acid  
 PSA = 3-pyridinesulfonic acid  
 PESA = 2-(4-pyridyl)-ethanesulfonic acid  
 RMOFs = rigid structural MOFs  
 Tz = 1H-1,2,4-triazole  
 TTFTB<sup>4-</sup> = tetrathiafulvalene-tetrabenzoate  
 TDHT = 2,4,6- tri(3,4-dihydroxyphenyl)-1,3,5-triazine  
 Im = imidazole

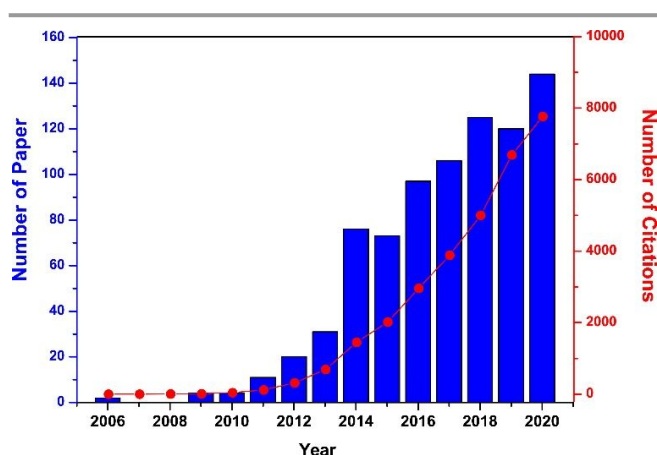


Fig 21. Statistical data for number of papers and citations of proton-conductive MOFs. The values were extracted from searching the proton-conductive MOFs in Web of Science.

anhydrous proton conductivity comparable to H<sub>2</sub>O media can be a target for the next proton-conductive MOFs. (6) For the improved mechanical strength of proton exchange membrane (PEM), the study of hybrid materials with MOFs and polymers is necessary. (7) A comprehensive understanding of the conduction mechanism using various tools is beneficial for designing new proton conductors.

### Conflicts of interest

There are no conflicts to declare.

### Acknowledgements

This research was supported by the ACCEL program, Japan Science and Technology Agency (JST), JPMJAC1501 and Grant-in-Aid for Specially Promoted Research (20H05623). D.-W Lim acknowledges that this work was supported by a National Research Foundation of Korea (NRF) grant funded by the Korea government (MSIT) (No. 2020R1G1A1101060).

### Notes and references

§ Abbreviations

- 1 A. Kirubakaran, S. Jain and R. K. Nema, *Renew. Sustain. Energy Rev.*, 2009, **13**, 2430–2440.
- 2 P. Colomban, *Solid State Ionics*, 2019, **334**, 125–144.
- 3 T. Program, E. Efficiency and R. Energy, *Office*, 2010, 1–105.
- 4 R. E. Rosli, A. B. Sulong, W. R. W. Daud, M. A. Zulkifley, T. Husaini, M. I. Rosli, E. H. Majlan and M. A. Haque, *Int. J. Hydrogen Energy*, 2017, **42**, 9293–9314.
- 5 Y. Shao, G. Yin, Z. Wang and Y. Gao, *J. Power Sources*, 2007, **167**, 235–242.
- 6 X. X. Wang, M. T. Swihart and G. Wu, *Nat. Catal.*, 2019, **2**, 578–589.
- 7 A. Chroneos, B. Yildiz, A. Tarancón, D. Parfitt and J. A. Kilner, *Energy Environ. Sci.*, 2011, **4**, 2774–2789.
- 8 J. R. Vinograd and J. W. McBain, *J. Am. Chem. Soc.*, 1941, **63**, 2008–2015.
- 9 P. Atkins and Ju. D. Paula, *Physical Chemistry*, W. H. Freeman and Company New York, 2nd edn., 2006.
- 10 E. S. Rogers and A. R. Ubbelohde, *Trans. Faraday Soc.*, 1950, **46**, 1051–1061.
- 11 K. A. Mauritz and R. B. Moore, *Chem. Rev.*, 2004, **104**, 4535–4585.

- 12 G. L. K. Hunter and W. B. Brogden, *J. Food Sci.*, 1985, **30**, 876–878.
- 13 W. Münch, K. D. Kreuer, U. Traub and J. Maier, *Solid State Ionics*, 1995, **77**, 10–14.
- 14 N. Kochetova, I. Animitsa, D. Medvedev, A. Demin and P. Tsiakaras, *RSC Adv.*, 2016, **6**, 73222–73268.
- 15 M. Sadakiyo, T. Yamada, K. Honda, H. Matsui and H. Kitagawa, *J. Am. Chem. Soc.*, 2014, **136**, 7701–7707.
- 16 M. Sadakiyo, T. Yamada and H. Kitagawa, *J. Am. Chem. Soc.*, 2009, **131**, 9906–9907.
- 17 M. Sadakiyo, T. Yamada and H. Kitagawa, *Chempluschem*, 2016, **81**, 691–701.
- 18 X. M. Li, L. Z. Dong, S. L. Li, G. Xu, J. Liu, F. M. Zhang, L. S. Lu and Y. Q. Lan, *ACS Energy Lett.*, 2017, **2**, 2313–2318.
- 19 C. Xiao, Y. Wang, L. Chen, X. Yin, J. Shu, D. Sheng, Z. Chai, T. E. Albrecht-Schmitt and S. Wang, *Chem. - A Eur. J.*, 2015, **21**, 17591–17595.
- 20 V. G. Ponomareva, K. A. Kovalenko, A. P. Chupakhin, D. N. Dybtsev, E. S. Shutova and V. P. Fedin, *J. Am. Chem. Soc.*, 2012, **134**, 15640–15643.
- 21 S. Liu, Z. Yue and Y. Liu, *Dalt. Trans.*, 2015, **44**, 12976–12980.
- 22 S. Bureekaew, S. Horike, M. Higuchi, M. Mizuno, T. Kawamura, D. Tanaka, N. Yanai and S. Kitagawa, *Nat. Mater.*, 2009, **8**, 831–836.
- 23 J. A. Hurd, R. Vaidhyanathan, V. Thangadurai, C. I. Ratcliffe, I. L. Moudrakovski and G. K. H. Shimizu, *Nat. Chem.*, 2009, **1**, 705–710.
- 24 V. G. Ponomareva, S. B. Aliev, E. S. Shutova, D. P. Pishchur, D. N. Dybtsev and V. P. Fedin, *RSC Adv.*, 2017, **7**, 403–407.
- 25 Y. Yoshida, K. Fujie, D.-W. Lim, R. Ikeda and H. Kitagawa, *Angew. Chemie - Int. Ed.*, 2019, **58**, 10909–10913.
- 26 Y. Yoshida and H. Kitagawa, *ACS Sustain. Chem. Eng.*, 2019, **7**, 70–81.
- 27 S. S. Bao, N. Z. Li, J. M. Taylor, Y. Shen, H. Kitagawa and L. M. Zheng, *Chem. Mater.*, 2015, **27**, 8116–8125.
- 28 S. S. Bao, K. Otsubo, J. M. Taylor, Z. Jiang, L. M. Zheng and H. Kitagawa, *J. Am. Chem. Soc.*, 2014, **136**, 9292–9295.
- 29 R. F. Mendes, P. Barbosa, E. M. Domingues, P. Silva, F. Figueiredo and F. A. Almeida Paz, *Chem. Sci.*, 2020, **11**, 6305–6311.
- 30 D. Umeyama, S. Horike, C. Tassel, H. Kageyama, Y. Higo, K. Hagi, N. Ogiwara and S. Kitagawa, *APL Mater.*, 2014, **2**, 124401.
- 31 D.-W. Lim and H. Kitagawa, *Chem. Rev.*, 2020, **120**, 8416–8467.
- 32 D. W. Lim, M. Sadakiyo and H. Kitagawa, *Chem. Sci.*, 2019, **10**, 16–33.
- 33 P. Ramaswamy, N. E. Wong and G. K. H. Shimizu, *Chem. Soc. Rev.*, 2014, **43**, 5913–5932.
- 34 Y. Ye, L. Gong, S. Xiang, Z. Zhang and B. Chen, *Adv. Mater.*, 2020, **32**, 1–28.
- 35 M. Yoon, K. Suh, S. Natarajan and K. Kim, *Angew. Chemie - Int. Ed.*, 2013, **52**, 2688–2700.
- 36 A. L. Li, Q. Gao, J. Xu and X. H. Bu, *Coord. Chem. Rev.*, 2017, **344**, 54–82.
- 37 X. Meng, H. N. Wang, S. Y. Song and H. J. Zhang, *Chem. Soc. Rev.*, 2017, **46**, 464–480.
- 38 H. Furukawa, N. Ko, Y. B. Go, N. Aratani, S. B. Choi, E. Choi, A. Ö. Yazaydin, R. Q. Snurr, M. O’Keeffe, J. Kim and O. M. Yaghi, *Science*, 2010, **329**, 424–428.
- 39 H. C. Zhou, J. R. Long and O. M. Yaghi, *Chem. Rev.*, 2012, **112**, 673–674.
- 40 O. K. Farha and J. T. Hupp, *Acc. Chem. Res.*, 2010, **43**, 1166–1175.
- 41 P. Z. Moghadam, A. Li, S. B. Wiggin, A. Tao, A. G. P. Maloney, P. A. Wood, S. C. Ward and D. Fairen-Jimenez, *Chem. Mater.*, 2017, **29**, 2618–2625.
- 42 H. Furukawa, K. E. Cordova, M. O’Keeffe and O. M. Yaghi, *Science*, 2013, **341**, 1230444.
- 43 H. Wang, Q.-L. Zhu, R. Zou and Q. Xu, *CHEM*, 2017, **2**, 52–80.
- 44 H. Li, K. Wang, Y. Sun, C. T. Lollar, J. Li and H. C. Zhou, *Mater. Today*, 2018, **21**, 108–121.
- 45 M. P. Suh, H. J. Park, T. K. Prasad and D.-W. Lim, *Chem. Rev.*, 2012, **112**, 782–835.
- 46 N. L. Rosi, J. Eckert, M. Eddaoudi, D. T. Vodak, J. Kim, M. O’Keeffe and O. M. Yaghi, *Science*, 2003, **300**, 1127–1129.
- 47 S. Ma and H. C. Zhou, *Chem. Commun.*, 2010, **46**, 44–53.
- 48 M. Shah, M. C. McCarthy, S. Sachdeva, A. K. Lee and H. K. Jeong, *Ind. Eng. Chem. Res.*, 2012, **51**, 2179–2199.
- 49 Y. Shi, B. Liang, R. B. Lin, C. Zhang and B. Chen, *Trends Chem.*, 2020, **2**, 254–269.
- 50 D. J. Babu, G. He, L. F. Villalobos and K. V. Agrawal, *ACS Sustain. Chem. Eng.*, 2019, **7**, 49–69.
- 51 K. Sumida, D. L. Rogow, J. A. Mason, T. M. McDonald, E. D. Bloch, Z. R. Herm, T. H. Bae and J. R. Long, *Chem. Rev.*, 2012, **112**, 724–781.
- 52 M. Ding, R. W. Flaig, H. L. Jiang and O. M. Yaghi, *Chem. Soc. Rev.*, 2019, **48**, 2783–2828.
- 53 J. R. Li, R. J. Kuppler and H. C. Zhou, *Chem. Soc. Rev.*, 2009, **38**, 1477–1504.
- 54 D. Britt, H. Furukawa, B. Wang, T. G. Glover and O. M. Yaghi, *Proc. Natl. Acad. Sci. U. S. A.*, 2009, **106**, 20637–20640.
- 55 L. Yang, S. Qian, X. Wang, X. Cui, B. Chen and H. Xing, *Chem. Soc. Rev.*, 2020, **49**, 5359–5406.
- 56 E. D. Bloch, W. L. Queen, R. Krishna, J. M. Zadrozny, C. M. Brown and J. R. T. Long, *Science*, 2012, **335**, 1606–1611.
- 57 J. Y. Kim, L. Zhang, R. Balderas-Xicohténcatl, J. Park, M. Hirscher, H. R. Moon and H. Oh, *J. Am. Chem. Soc.*, 2017, **139**, 17743–17746.
- 58 J. Y. Kim, H. Oh and H. R. Moon, *Adv. Mater.*, 2019, **31**, 1–23.
- 59 M. X. Wu and Y. W. Yang, *Adv. Mater.*, 2017, **29**, 1606134.
- 60 A. C. McKinlay, R. E. Morris, P. Horcajada, G. Férey, R. Gref, P. Couvreur and C. Serre, *Angew. Chemie - Int. Ed.*, 2010, **49**, 6260–6266.
- 61 D. Farrusseng, S. Aguado and C. Pinel, *Angew. Chemie - Int. Ed.*, 2009, **48**, 7502–7513.
- 62 A. Dhakshinamoorthy, Z. Li and H. Garcia, *Chem. Soc. Rev.*, 2018, **47**, 8134–8172.

- 63 H. R. Moon, D. W. Lim and M. P. Suh, *Chem. Soc. Rev.*, 2013, **42**, 1807–1824.
- 64 D.-W. Lim, J. W. Yoon, K. Y. Ryu and M. P. Suh, *Angew. Chemie Int. Ed.*, 2012, **51**, 9814–9817.
- 65 M. P. Suh, H. R. Moon, E. Y. Lee and S. Y. Jang, *J. Am. Chem. Soc.*, 2006, **128**, 4710–4718.
- 66 H. R. Moon, J. H. Kim and M. P. Suh, *Angew. Chemie - Int. Ed.*, 2005, **44**, 1261–1265.
- 67 Z. Meng, R. M. Stolz, L. Mendecki and K. A. Mirica, *Chem. Rev.*, 2019, **119**, 478–598.
- 68 X. Wang, T. Qin, S. S. Bao, Y. C. Zhang, X. Shen, L. M. Zheng and D. Zhu, *J. Mater. Chem. A*, 2016, **4**, 16484–16489.
- 69 K. Guo, L. Zhao, S. Yu, W. Zhou, Z. Li and G. Li, *Inorg. Chem.*, 2018, **57**, 7104–7112.
- 70 M. G. Campbell, D. Sheberla, S. F. Liu, T. M. Swager and M. Dincă, *Angew. Chemie - Int. Ed.*, 2015, **54**, 4349–4352.
- 71 D. Sheberla, J. C. Bachman, J. S. Elias, C. J. Sun, Y. Shao-Horn and M. Dincă, *Nat. Mater.*, 2017, **16**, 220–224.
- 72 S. Kanda, K. Yamashita and K. Ohkawa, *Bull. Chem. Soc. Jpn.*, 1979, **52**, 3296–3301.
- 73 Y. Nagao, M. Fujishima, R. Ikeda, S. Kanda and H. Kitagawa, *Synth. Met.*, 2003, **133–134**, 431–432.
- 74 Y. Nagao, T. Kubo, K. Nakasuji, R. Ikeda, T. Kojima and H. Kitagawa, *Synth. Met.*, 2005, **154**, 89–92.
- 75 M. Sadakiyo, T. Yamada and H. Kitagawa, *J. Am. Chem. Soc.*, 2009, **131**, 9906–9907.
- 76 F. Yang, G. Xu, Y. Dou, B. Wang, H. Zhang, H. Wu, W. Zhou, J. R. Li and B. Chen, *Nat. Energy*, 2017, **2**, 877–883.
- 77 M. Sadakiyo, H. Okawa, A. Shigematsu, M. Ohba, T. Yamada and H. Kitagawa, *J. Am. Chem. Soc.*, 2012, **134**, 5472–5475.
- 78 A. Shigematsu, T. Yamada and H. Kitagawa, *J. Am. Chem. Soc.*, 2011, **133**, 2034–2036.
- 79 T. Yamada, M. Sadakiyo and H. Kitagawa, *J. Am. Chem. Soc.*, 2009, **131**, 3144–3145.
- 80 M. K. Sarango-Ramírez, D.-W. Lim, D. I. Kolokolov, A. E. Khudozhitkov, A. G. Stepanov and H. Kitagawa, *J. Am. Chem. Soc.*, 2020, **142**, 6861–6865.
- 81 Y. Ye, W. Guo, L. Wang, Z. Li, Z. Song, J. Chen, Z. Zhang, S. Xiang and B. Chen, *J. Am. Chem. Soc.*, 2017, **139**, 15604–15607.
- 82 N. C. Jeong, B. Samanta, C. Y. Lee, O. K. Farha and J. T. Hupp, *J. Am. Chem. Soc.*, 2012, **134**, 51–54.
- 83 W. J. Phang, H. Jo, W. R. Lee, J. H. Song, K. Yoo, B. Kim and C. S. Hong, *Angew. Chemie - Int. Ed.*, 2015, **54**, 5142–5146.
- 84 V. G. Ponomareva, K. A. Kovalenko, A. P. Chupakhin, D. N. Dybtsev, E. S. Shutova and V. P. Fedin, *J. Am. Chem. Soc.*, 2012, **134**, 15640–15643.
- 85 I. J. Kang, N. A. Khan, E. Haque and S. H. Jung, *Chem. - A Eur. J.*, 2011, **17**, 6437–6442.
- 86 T. Kajiwara, M. Higuchi, D. Watanabe, H. Higashimura, T. Yamada and H. Kitagawa, *Chem. - A Eur. J.*, 2014, **20**, 15611–15617.
- 87 J. Duan, W. Jin and S. Kitagawa, *Coord. Chem. Rev.*, 2017, **332**, 48–74.
- 88 A. J. Rieth and M. Dinca, *J. Am. Chem. Soc.*, 2018, **140**, 3461–3466.
- 89 V. Colombo, S. Galli, H. J. Choi, G. D. Han, A. Maspero, G. Palmisano, N. Masciocchi and J. R. Long, *Chem. Sci.*, 2011, **2**, 1311–1319.
- 90 H. J. Choi, M. Dincă, A. Dailly and J. R. Long, *Energy Environ. Sci.*, 2010, **3**, 117–123.
- 91 E. Pardo, C. Train, G. Gontard, K. Boubekeur, O. Fabelo, H. Liu, B. Dkhil, F. Lloret, K. Nakagawa, H. Tokoro, S. I. Ohkoshi and M. Verdaguier, *J. Am. Chem. Soc.*, 2011, **133**, 15328–15331.
- 92 Y. S. Wei, X. P. Hu, Z. Han, X. Y. Dong, S. Q. Zang and T. C. W. Mak, *J. Am. Chem. Soc.*, 2017, **139**, 3505–3512.
- 93 S. Wang, M. Wahiduzzaman, L. Davis, A. Tissot, W. Shepard, J. Marrot, C. Martineau-Corcoc, D. Hamdane, G. Maurin, S. Devautour-Vinot and C. Serre, *Nat. Commun.*, 2018, **9**, 1–8.
- 94 T. Islamoglu, S. Goswami, Z. Li, A. J. Howarth, O. K. Farha and J. T. Hupp, *Acc. Chem. Res.*, 2017, **50**, 805–813.
- 95 Y. K. Hwang, D. Y. Hong, J. S. Chang, S. H. Jung, Y. K. Seo, J. Kim, A. Vimont, M. Daturi, C. Serre and G. Férey, *Angew. Chemie - Int. Ed.*, 2008, **47**, 4144–4148.
- 96 P. Deria, J. E. Mondloch, E. Tylianakis, P. Ghosh, W. Bury, R. Q. Snurr, J. T. Hupp and O. K. Farha, *J. Am. Chem. Soc.*, 2013, **135**, 16801–16804.
- 97 C. Chen, Z. Wu, Y. Que, B. Li, Q. Guo, Z. Li, L. Wang, H. Wan and G. Guan, *RSC Adv.*, 2016, **6**, 54119–54128.
- 98 S. M. Cohen, *Chem. Rev.*, 2012, **112**, 970–1000.
- 99 K. K. Tanabe and S. M. Cohen, *Chem. Soc. Rev.*, 2011, **40**, 498–519.
- 100 J. Canivet, S. Aguado, Y. Schuurman and D. Farrusseng, *J. Am. Chem. Soc.*, 2013, **135**, 4195–4198.
- 101 Y. Luan, N. Zheng, Y. Qi, J. Yu and G. Wang, *Eur. J. Inorg. Chem.*, 2014, **2014**, 4268–4272.
- 102 J. Lee, D. W. Lim, S. Dekura, H. Kitagawa and W. Choe, *ACS Appl. Mater. Interfaces*, 2019, **11**, 12639–12646.
- 103 D. Umeyama, S. Horike, M. Inukai, Y. Hijikata and S. Kitagawa, *Angew. Chemie - Int. Ed.*, 2011, **50**, 11706–11709.
- 104 C. Montoro, P. Ocñ, F. Zamora and J. A. R. Navarro, *Chem. - A Eur. J.*, 2016, **22**, 1646–1651.
- 105 J. Ren, M. Ledwaba, N. M. Musyoka, H. W. Langmi, M. Mathe, S. Liao and W. Pang, *Coord. Chem. Rev.*, 2017, **349**, 169–197.
- 106 J. M. Taylor, S. Dekura, R. Ikeda and H. Kitagawa, *Chem. Mater.*, 2015, **27**, 2286–2289.
- 107 J. M. Taylor, T. Komatsu, S. Dekura, K. Otsubo, M. Takata and H. Kitagawa, *J. Am. Chem. Soc.*, 2015, **137**, 11498–11506.
- 108 M. Inukai, S. Horike, T. Itakura, R. Shinozaki, N. Ogiwara, D. Umeyama, S. Nagarkar, Y. Nishiyama, M. Malon, A. Hayashi, T. Ohhara, R. Kiyanagi and S. Kitagawa, *J. Am. Chem. Soc.*, 2016, **138**, 8505–8511.
- 109 D. I. Kolokolov, D.-W. Lim and H. Kitagawa, *Chem. Rec.*, 2020, **20**, 1–18.
- 110 N. Agmon, *Chem. Phys. Lett.*, 1995, **244**, 456–462.
- 111 K. Kreuer, A. Rabenau and W. Weppner, *Angew. Chemie - Int. Ed.*, 1982, **21**, 208–209.

- 112 F. Jaouen, E. Proietti, M. Lefèvre, R. Chenitz, J. P. Dodelet, G. Wu, H. T. Chung, C. M. Johnston and P. Zelenay, *Energy Environ. Sci.*, 2011, **4**, 114–130.
- 113 M. F. H. Schuster and W. H. Meyer, *Annu. Rev. Mater. Res.*, 2003, **33**, 233–261.
- 114 K. D. Kreuer, S. J. Paddison, E. Spohr and M. Schuster, *Chem. Rev.*, 2004, **104**, 4637–4678.
- 115 A. Kawada, A. R. McGhie and M. M. Labes, *J. Chem. Phys.*, 1970, **52**, 3121–3125.
- 116 S. Horike, D. Umeyama, M. Inukai, T. Itakura and S. Kitagawa, *J. Am. Chem. Soc.*, 2012, **134**, 7612–7615.
- 117 C. R. Li, S. Li and X. M. Zhang, *Cryst. Growth Des.*, 2009, **9**, 1702–1707.
- 118 S. S. Nagarkar, S. M. Unni, A. Sharma, S. Kurungot and S. K. Ghosh, *Angew. Chemie - Int. Ed.*, 2014, **53**, 2638–2642.
- 119 X. M. Li, L. Z. Dong, J. Liu, W. X. Ji, S. L. Li and Y. Q. Lan, *Chem*, 2020, **6**, 2272–2282.
- 120 C. K. Brozek and M. Dincă, *Chem. Soc. Rev.*, 2014, **43**, 5456–5467.
- 121 J. G. Park, M. L. Aubrey, J. Oktawiec, K. Chakarawet, L. E. Darago, F. Grandjean, G. J. Long and J. R. Long, *J. Am. Chem. Soc.*, 2018, **140**, 8526–8534.
- 122 C. K. Brozek and M. Dincă, *J. Am. Chem. Soc.*, 2013, **135**, 12886–12891.
- 123 L. S. Xie, G. Skorupskii and M. Dincă, *Chem. Rev.*, 2020, **120**, 8536–8580.
- 124 X. Zhang, Z. Chen, X. Liu, S. L. Hanna, X. Wang, R. Taheri-Ledari, A. Maleki, P. Li and O. K. Farha, *Chem. Soc. Rev.*, 2020, **49**, 7406–7427.
- 125 Ü. Kökçam-Demir, A. Goldman, L. Esrafilı, M. Gharib, A. Morsali, O. Weingart and C. Janiak, *Chem. Soc. Rev.*, 2020, **49**, 2751–2798.
- 126 S. S. Liu, Z. Han, J. Sen Yang, S. Z. Huang, X. Y. Dong and S. Q. Zang, *Inorg. Chem.*, 2020, **59**, 396–402.
- 127 C. Serre, C. Mellot-Draznieks, S. Surblé, N. Audebrand, Y. Filinchuk, G. Férey and An, *Science*, 2007, **315**, 1828–1832.
- 128 F. M. Zhang, L. Z. Dong, J. S. Qin, W. Guan, J. Liu, S. L. Li, M. Lu, Y. Q. Lan, Z. M. Su and H. C. Zhou, *J. Am. Chem. Soc.*, 2017, **139**, 6183–6189.
- 129 W. J. Phang, W. R. Lee, K. Yoo, D. W. Ryu, B. Kim and C. S. Hong, *Angew. Chemie - Int. Ed.*, 2014, **53**, 8383–8387.
- 130 S. Hwang, E. J. Lee, D. Song and N. C. Jeong, *ACS Appl. Mater. Interfaces*, 2018, **10**, 35354–35660.
- 131 J. Pang, F. Jiang, M. Wu, C. Liu, K. Su, W. Lu, D. Yuan and M. Hong, *Nat. Commun.*, 2015, **6**, 7575.
- 132 K. M. Choi, H. J. Jeon, J. K. Kang and O. M. Yaghi, *J. Am. Chem. Soc.*, 2011, **133**, 11920–11923.
- 133 M. Kim, J. F. Cahill, H. Fei, K. A. Prather and S. M. Cohen, *J. Am. Chem. Soc.*, 2012, **134**, 18082–18088.
- 134 L. P. Hammett, *J. Am. Chem. Soc.*, 1937, **59**, 96–103.
- 135 T. Yamada, Y. Shirai and H. Kitagawa, *Chem. - An Asian J.*, 2014, **9**, 1316–1320.
- 136 D. N. Dybtsev, V. G. Ponomareva, S. B. Aliev, A. P. Chupakhin, M. R. Gallyamov, N. K. Moroz, B. A. Kolesov, K. A. Kovalenko, E. S. Shutova and V. P. Fedin, *ACS Appl. Mater. Interfaces*, 2014, **6**, 5161–5167.
- 137 X. Y. Dong, J. J. Li, Z. Han, P. G. Duan, L. K. Li and S. Q. Zang, *J. Mater. Chem. A*, 2017, **5**, 3464–3474.
- 138 S. S. Park, A. J. Rieth, C. H. Hendon and M. Dincă, *J. Am. Chem. Soc.*, 2018, **140**, 2016–2019.
- 139 S. Chand, S. C. Pal, D.-W. Lim, K. Otsubo, A. Pal, H. Kitagawa and M. C. Das, *ACS Mater. Lett.*, 2020, **2**, 1343–1350.
- 140 D. Umeyama, S. Horike, M. Inukai and S. Kitagawa, *J. Am. Chem. Soc.*, 2013, **135**, 11345–11350.
- 141 P. Ramaswamy, N. E. Wong, B. S. Gelfand and G. K. H. Shimizu, *J. Am. Chem. Soc.*, 2015, **137**, 7640–7643.
- 142 Z. Hassanzadeh Fard, N. E. Wong, C. D. Malliakas, P. Ramaswamy, J. M. Taylor, K. Otsubo and G. K. H. Shimizu, *Chem. Mater.*, 2018, **30**, 314–318.
- 143 S. M. Elahi, S. Chand, W. H. Deng, A. Pal and M. C. Das, *Angew. Chemie - Int. Ed.*, 2018, **57**, 6662–6666.
- 144 H. Wu, F. Yang, X. L. Lv, B. Wang, Y. Z. Zhang, M. J. Zhao and J. R. Li, *J. Mater. Chem. A*, 2017, **5**, 14525–14529.
- 145 H. Ōkawa, K. Otsubo, Y. Yoshida and H. Kitagawa, *Chem. Commun.*, 2020, **56**, 6138–6140.
- 146 K. Otake, K. Otsubo, T. Komatsu, S. Dekura, J. M. Taylor, R. Ikeda, K. Sugimoto, A. Fujiwara, C. P. Chou, A. W. Sakti, Y. Nishimura, H. Nakai and H. Kitagawa, *Nat. Commun.*, 2020, **11**, 843.
- 147 M. Bazaga-García, R. M. P. Colodrero, M. Papadaki, P. Garczarek, J. Zorń, P. Olivera-Pastor, E. R. Losilla, L. León-Reina, M. A. G. Aranda, D. Choquesillo-Lazarte, K. D. Demadis and A. Cabeza, *J. Am. Chem. Soc.*, 2014, **136**, 5731–5739.
- 148 J. Cao, W. Ma, K. Lyu, L. Zhuang, H. Cong and H. Deng, *Chem. Sci.*, 2020, **11**, 3978–3985.
- 149 H. G. Park and Y. Jung, *Chem. Soc. Rev.*, 2014, **43**, 565–576.
- 150 S. S. Bao, G. K. H. Shimizu and L. M. Zheng, *Coord. Chem. Rev.*, 2019, **378**, 577–594.
- 151 G. K. H. Shimizu, R. Vaidhyanathan and J. M. Taylor, *Chem. Soc. Rev.*, 2009, **38**, 1430–1449.
- 152 X. X. Xie, Y. C. Yang, B. H. Dou, Z. F. Li and G. Li, *Coord. Chem. Rev.*, 2020, **403**, 213100.